My paper on the cosmic microwave background and formation of structures in our Universe

V. A. Vikenes[1]

Institute of Theoretical Astrophysics, University of Oslo, 0315 Oslo, Norway
e-mail: v.a.vikenes@astro.uio.no

June 1, 2023

ABSTRACT

The code for this project can be found on my GitHub repository: https://github.com/Vikenes/AST5220/

1. Introduction

In this report our goal is to compute the angular power spectrum of the cosmic microwave background (CMB) radiation. In Sect. 3 we compute the background cosmology, determining the evolution of the Universe in general. Sect. 4 focuses on the behaviour of particles in the Universe, mainly focusing on production of neutral Hydrogen. In Sect. 5 we consider cosmological perturbation theory, and study how tiny perturbation of the content of the Universe evolves on different scales. Finally, in Sect. 6, we use the perturbation quantities to compute the CMB power spectrum.

Throughout this paper, we will use cosmological parameters from the latest Planck data Planck2020, unless otherwise mentioned,

2. Fiducial parameters

The parameter values we use in this report are

$$
\begin{aligned}
h &= 0.67, \\
T_{\mathrm{CMB0}} &= 2.7255\,\mathrm{K}, \\
\mathcal{N}_{\mathrm{eff}} &= 3.046, \\
\Omega_{b0} &= 0.05, \\
\Omega_{\mathrm{CDM0}} &= 0.267, \\
\Omega_{k0} &= 0, \\
\Omega_{\nu0} &= \mathcal{N}_{\mathrm{eff}} \cdot \frac{7}{8}\left(\frac{4}{11}\right)^{4/3} \Omega_{\gamma0}, \\
\Omega_{\Lambda0} &= 1 - (\Omega_{k0} + \Omega_{b0} + \Omega_{\mathrm{CDM0}} + \Omega_{\gamma0} + \Omega_{\nu0}), \\
n_s &= 0.965, \\
A_s &= 2.1 \cdot 10^{-9}, \\
Y_p &= 0.245, \\
z_{\mathrm{reion}} &= 8, \\
\Delta z_{\mathrm{reion}} &= 0.5, \\
z_{\mathrm{Hereion}} &= 3.5, \\
\Delta z_{\mathrm{Hereion}} &= 0.5,
\end{aligned}
\tag{1}
$$

3. Milestone I

In this section we will examine the evolution of the Universe's uniform background. Our primary objective is to develop methods for computing the Hubble parameter and related time- and distance measures. These methods provide a first step towards further investigations and modelling of the early Universe. To compute the background cosmology, we will solve ordinary differential equations (ODEs) numerically, using cosmological parameters obtained from the Planck Collaboration (Planck Collaboration et al. 2020). The parameters we will use are listed in Eq. (1) in Appendix 2. One crucial aspect in the process is validating our model. We will therefore develop some simple methods for comparing our result. This will mainly involve considering simplified cases where analytical solutions can be obtained.

Our primary focus in this section concerns methods where the cosmological parameters are given from the start. Another interesting aspect is to use data to constrain cosmological parameters. To do this, we will use data from supernova observations (Betoule et al. 2014), containing luminosity distance associated with different values of redshift. By employing the numerical methods we develop initially, we will try to estimate optimal values of three cosmological parameters, by implement a simple Markov chain Monte Carlo (MCMC) algorithm. The parameters we will be sampling are h, Ω_{m0} and Ω_{k0}. From these results, we will investigate confidence regions of Ω_{m0} and $\Omega_{\Lambda0}$, and try to estimate a probability distribution function (PDF) for the Hubble parameter.

3.1. Theory

3.1.1. Density parameters and Hubble factor

The Friedmann equation can be written in terms of density parameters, $\Omega_i \equiv \rho_i/\rho_c$, where $\rho_c \equiv 3H^2/8\pi G$ is the critical density. The density of a given species, i, evolves as (Dodelson 2020, Eq. (2.61))

$$
\rho_i(t) \propto a(t)^{-3(1+w_i)}, \tag{2}
$$

where we have assumed that the equation of state (EoS) parameter, $w_i \equiv P_i/\rho_i$ (Dodelson 2020, Eq. 2.60), is constant. P_i

denotes the pressure of the species. We will limit ourselves to consider three types of species in this report: matter, radiation and dark energy. We will only consider baryons and cold dark matter (CDM) for the matter component, which we express as $\Omega_{m0} = \Omega_{b0} + \Omega_{CDM0}$. The subscript 0 is used to refer to today's value. The radiation component we consider is $\Omega_{r0} = \Omega_{\gamma0} + \Omega_{\nu0}$, corresponding to photons and neutrinos, respectively. For the dark energy, we only have the cosmological constant $\Omega_{\Lambda0}$.

Matter, radiation and dark energy have densities evolving according to Eq. (2) with $w_i = 0$, $1/3$ and -1, respectively. Neutrinos having $w = 1/3$ only holds since we will assume that the neutrinos are massless. Curvature can be described by $w_i = -1/3$, with $\Omega_{k0} \equiv -kc^2/H_0^2$. The parameter k represents the curvature of the Universe, where $k = 0$ corresponds to a flat Universe. With these parameters, the Friedmann Equation can be written as (Dodelson 2020, Eq. (3.14))

$$H = H_0 \sqrt{\Omega_{m0}a^{-3} + \Omega_{r0}a^{-4} + \Omega_{k0}a^{-2} + \Omega_{\Lambda0}}, \tag{3}$$

where $H \equiv \dot{a}/a$ is the Hubble parameter, with the dot denoting a derivative with respect to cosmic time, t. For the radiation, $\Omega_{\gamma0}$ and $\Omega_{\nu0}$ follow from the temperature of the CMB today, T_{CMB0}, and the effective number of massless neutrinos, $\mathcal{N}_{eff}$. They are given by

$$\Omega_{\gamma0} = 2 \cdot \frac{\pi^2}{30} \frac{(k_b T_{CMB0})^4}{\hbar^3 c^5} \cdot \frac{8\pi G}{3H_0^2}, \tag{4}$$

$$\Omega_{\nu0} = \mathcal{N}_{eff} \cdot \frac{7}{8} \cdot \left(\frac{4}{11}\right)^{4/3} \Omega_{\gamma0}. \tag{5}$$

The value of $\Omega_{\Lambda0}$ is fixed by the requirement that $H(a = 1) = H_0$, yielding

$$\Omega_{\Lambda0} = 1 - (\Omega_{m0} + \Omega_{r0} + \Omega_{k0}). \tag{6}$$

We also introduce the scaled Hubble factor, $\mathcal{H} \equiv aH$. Rather than working with the scale factor, $a(t)$, we will mainly be working with the logarithm of the scale factor

$$x \equiv \ln a, \quad ' \equiv \frac{d}{dx}. \tag{7}$$

The resulting expression for $\mathcal{H}(x)$ is thus

$$\mathcal{H}(x) = H_0 \sqrt{\Omega_{m0}e^{-x} + \Omega_{r0}e^{-2x} + \Omega_{k0} + \Omega_{\Lambda0}e^{2x}}. \tag{8}$$

This form of the Hubble factor is the one we will focus on for the majority of this report. In terms of $\mathcal{H}(x)$, the value of the density parameters can be obtained at any given x, with

$$\Omega_k(x) = \frac{\Omega_{k0}}{\mathcal{H}(x)^2/H_0^2}, \tag{9}$$

$$\Omega_m(x) = \frac{\Omega_{m0}}{e^x\mathcal{H}(x)^2/H_0^2}, \tag{10}$$

$$\Omega_r(x) = \frac{\Omega_{r0}}{e^{2x}\mathcal{H}(x)^2/H_0^2}, \tag{11}$$

$$\Omega_\Lambda(x) = \frac{\Omega_{\Lambda0}}{e^{-2x}\mathcal{H}(x)^2/H_0^2}, \tag{12}$$

From these expressions, we can identify the epochs during which the Universe was dominated by an equal amount of matter and radiation, and by an equal amount of matter and dark energy. These epochs are defined by the time when $\Omega_m = \Omega_r$

and $\Omega_m = \Omega_\Lambda$, respectively, and are a valuable asset towards understanding the physics governing the evolution of the Universe. Another time of interest is the onset of acceleration, defined as the time when $\ddot{a} = 0$. In terms of $\mathcal{H}$ and x, this corresponds to

$$\ddot{a} = \frac{dx}{dt}\frac{d\dot{a}}{dx} = \frac{d\ln a}{dt}\frac{d\mathcal{H}(x)}{dx} = e^{-x}\mathcal{H}(x)\frac{d\mathcal{H}(x)}{dx}. \tag{13}$$

In Sect. 3.1.4 we will derive an expression for $\mathcal{H}'(x)$.

3.1.2. Conformal time

We now want to relate the Hubble factor to some time variables. The main one we will consider is the conformal time, η. It is a measure of the distance light has been able to travel since $t = 0$, where t is the cosmic time. Using its definition in terms of t (Dodelson 2020, Eq. (2.90)), we can express it in terms of x as

$$\eta = \int_0^t \frac{c\,dt'}{a(t')} = \int_{-\infty}^{x'} \frac{c\,dx'}{\mathcal{H}(x')}. \tag{14}$$

This leads us to the following differential equation that we will solve numerically

$$\frac{d\eta}{dx} = \frac{c}{\mathcal{H}(x)}. \tag{15}$$

The initial condition we have is $\eta(-\infty) = 0$. Noting from Eq. (8) that $\mathcal{H}(x) \to H_0 \sqrt{\Omega_{r0}}e^{-x}$ as $x \to -\infty$, we get an analytical approximation for the initial condition of η at early times

$$\eta(x_{start}) \approx \int_{-\infty}^{x_{start}} \frac{c\,dx'}{H_0 \sqrt{\Omega_{r0}}}e^{x'} = \frac{c}{\mathcal{H}(x_{start})}. \tag{16}$$

Note that $\eta(x)\mathcal{H}(x)/c \to 1$ at low x, which provides a natural way of validating our implementation. $\eta(x)$ is related to the particle horizon, which is the comoving distance light could have travelled since the Big Bang, which equals ηc. It is therefore often referred to as the comoving horizon, as it determines the scale over which there have been causal contact in the Universe. This will have great impact on how structures grow in the early Universe, as we shall see in Sect. 5 and Sect. 6. Its value today, $\eta_0 \equiv \eta(t_0)$, represents the furthest distance from which we can receive information from the past, and it therefore defines the observable Universe.

For the cosmic time, t, starting from $H = \dot{a}/a$ and applying the chain rule yields the desired differential equation for $t(x)$, which we will solve numerically,

$$\frac{dt}{dx} = \frac{1}{H(x)}. \tag{17}$$

To get an initial condition for t, we consider the radiation dominating era, with the following integral expression

$$t(x) = \int_{-\infty}^x \frac{dx'}{H(x')}. \tag{18}$$

Comparing with Eq. (16), we see that the two integrands only differ by a factor e^x. The initial condition for t is therefore easily seen to be

$$t(x_{start}) = \frac{1}{2H(x_{start})}. \tag{19}$$

3.1.3. Distance measures

The supernova data we will study has distances measured in terms of luminosity distance, d_L. Expressing it in terms of the angular distance, $d_A = ar$, it becomes

$$d_L(a) = \frac{d_A}{a^2} = \frac{r}{a} \implies d_L(x) = e^{-x}r. \tag{20}$$

Here, r represents the radial coordinate of the emitted photon. To get an expression for r, we consider a photon's line-element in spherical coordinates,

$$ds^2 = -c^2dt^2 + a^2\left(\frac{dr^2}{1 - kr^2} + r^2d\theta^2 + r^2\sin^2\theta d\phi^2\right). \tag{21}$$

For photons travelling radially towards us, we have $d\theta = d\phi = 0$. Since $ds^2 = 0$ for photons, integrating the line-element of a photon emitted at, (t, r), reaching an observer at $(t_0, 0)$, yields

$$\int_0^r \frac{dr'}{\sqrt{1 - kr'}} = \int_t^{t_0} \frac{c\,dt}{a}. \tag{22}$$

The RHS of Eq. (22) is known as the co-moving distance, χ, which in terms of conformal time is given as

$$\chi = \int_t^{t_0} \frac{c\,dt}{a} = \int_x^0 \frac{c\,dx'}{\mathcal{H}(x')} = \eta(0) - \eta(x). \tag{23}$$

Solving Eq. (22) with respect to r, we get

$$r = \begin{cases} \chi \cdot \frac{\sin\left(\sqrt{|\Omega_{k0}|}H_0\chi/c\right)}{\left(\sqrt{|\Omega_{k0}|}H_0\chi/c\right)}, & \Omega_{k0} < 0, \\ \chi, & \Omega_{k0} = 0, \\ \chi \cdot \frac{\sinh\left(\sqrt{|\Omega_{k0}|}H_0\chi/c\right)}{\left(\sqrt{|\Omega_{k0}|}H_0\chi/c\right)}, & \Omega_{k0} > 0. \end{cases} \tag{24}$$

Eq. (20) can now be used to compute d_L, and the expression to use depends on the curvature.

3.1.4. Analytical solutions

In Sect. 3.1.2 we discussed how $\eta(x)$ can be used to test our implementation in the radiation dominating era. To test our solutions in other regimes, we will need the first and second derivative of $\mathcal{H}(x)$. To simplify the resulting expressions, we define the function, $g(x)$, as the derivative of the term inside the square root in Eq. (8), namely

$$g(x) \equiv -\Omega_{m0}e^{-x} - 2\Omega_{r0}e^{-2x} + 2\Omega_{\Lambda0}e^{2x}. \tag{25}$$

The first two derivatives of $\mathcal{H}(x)$ are easily seen to be

$$\frac{d\mathcal{H}(x)}{dx} = \frac{H_0^2}{2\mathcal{H}(x)}g(x), \tag{26}$$

$$\frac{d^2\mathcal{H}(x)}{dx^2} = \frac{H_0^2}{2\mathcal{H}(x)}\left[g'(x) - \frac{1}{2}\left(\frac{H_0g(x)}{\mathcal{H}(x)}\right)^2\right]. \tag{27}$$

Now we will consider the situation where the Universe is dominated by a single fluid with a constant EoS parameter, w. In that case we have $H(t)^2 \propto \rho_i(t)^2$ (Dodelson 2020, Eq. (3.13)). Using Eq. (2), the Hubble parameter expressed in terms of w_i becomes

$$H(t)^2 \propto a^{-3(1+w)} \implies \mathcal{H}(x) = c_1e^{-\frac{3}{2}(1+w)x}, \tag{28}$$

where c_1 is some constant. The reason for doing this, is that both c_1 and the exponential factor drops out when we consider $\mathcal{H}'(x)/\mathcal{H}(x)$ and $\mathcal{H}''(x)/\mathcal{H}(x)$. For different values of w_i, $\mathcal{H}'(x)/\mathcal{H}(x)$ becomes

$$\frac{1}{\mathcal{H}(x)}\frac{d\mathcal{H}}{dx} = -\frac{1 + 3w}{2} = \begin{cases} -1, & w = 1/3, \\ -1/2, & w = 0, \\ 1, & w = -1. \end{cases} \tag{29}$$

Similarly, the expression for $\mathcal{H}''(x)/\mathcal{H}(x)$ becomes

$$\frac{1}{\mathcal{H}(x)^2}\frac{d^2\mathcal{H}}{dx^2} = \frac{(1 + 3w)^2}{2} = \begin{cases} 1, & w = 1/3 \\ 1/4, & w = 0 \\ 1, & w = -1 \end{cases} \tag{30}$$

Equations (29) and (30) offer a means to evaluate the accuracy of our numerical solution at different regimes. Each density parameter evolve differently with x, as seen from Eqs. (9)-(12). Certain ranges of x-values will therefore closely resemble a Universe that is dominated by a single fluid. By computing $\mathcal{H}$, $\mathcal{H}'$, and $\mathcal{H}''$, we can examine whether these quantities exhibit the expected behaviour. This allows us to assess the validity of our model and ensure that it is consistent with the underlying physical principles.

3.2. Implementation details

To solve the differential equations for η and t (Eq. (15) and (17)) we use the C++ library GSL Galassi (2009), and use their Runge-Kutta4 solver. From the solution we create a spline of the results for the given x domain we have considered.

We will consider three different ranges of x-values. For the initial testing, we will use $x \in [\ln 10^{-10}, 5]$. For fitting cosmological parameters to the supernova data, we will use $x \in [\ln 10^{-2}, 0]$. When we want to estimate important times during the cosmic evolution, we will consider $x \in [-10, 1]$, for increased resolution, as the result may vary by a noticeable amount between step sizes. In all cases, we use $N_x = 10^5$ number of points.

The cosmological parameters we consider assume $\Omega_{k0} = 0$. In Sect. 3.2.1 we discuss how we will use supernova data to estimate a value for Ω_{k0}. Curvature is therefore implemented in all the relevant methods, but we set $\Omega_{k0} = 0$ when we're not dealing with supernova fitting.

3.2.1. Supernova fitting and parameter sampling

The supernova data we will use contains $N = 31$ data points of luminosity distance, $d_L^{\text{obs}}(z_i)$, with associated measurement errors, σ_i, at different redshifts, $z_i \in [0.01, 1.30]$. Using these measurements, we want to constrain the three-dimensional parameter space

$$C = \left\{\hat{h}, \hat{\Omega}_{m0}, \hat{\Omega}_{k0}\right\}, \tag{31}$$

where the hat is used to distinguish the estimated parameters from the fiducial ones. We set $\Omega_{b0} = 0.05$, although its particular value is irrelevant for this analysis, which is only sensitive to $\hat{\Omega}_{m0} = \Omega_{CDM0} + \Omega_{b0}$. Choosing a value for Ω_{b0} means that $\hat{\Omega}_{m0}$ enters via $\Omega_{CDM0} = \hat{\Omega}_{m0} - \Omega_{b0}$. Additionally, the small scales we probe here means that neutrinos are irrelevant, since we are well within matter domination, as we will see in Sect. 3.3.1. We therefore set $\mathcal{N}_{\text{eff}} = 0$ for this analysis.

We will assume that the measurements at different redshifts are normal distributed and uncorrelated. The likelihood function is then given by $L \propto e^{-\chi^2/2}$, where

$$\chi^2(C) = \sum_{i=1}^{N} \frac{[d_L(z_i, C) - d_L^{\text{obs}}(z_i)]^2}{\sigma_i^2}, \tag{32}$$

is the function we want to minimize. To do this, we will sample parameter values randomly by a Markov chain Monte Carlo (MCMC) process. We also restrict the parameter space to sample, with the following limits:

$$0.5 < \hat{h} < 1.5,$$
$$0 < \hat{\Omega}_{m0} < 1,$$
$$-1 < \hat{\Omega}_{k0} < 1. \tag{33}$$

To generate a new sample, we update each parameter by generating a random number $P \sim \mathcal{N}(0, 1)$, and multiplying it by a step size. We will use step sizes of $\Delta \hat{h} = 0.007, \Delta \hat{\Omega}_{m0} = 0.05, \Delta \hat{\Omega}_{k0} = 0.05$. To determine whether a new configuration should be included in the sample we use the Metropolis algorithm, where we always accept a state if it yields a lower value of χ^2 compared to the previous state that was accepted. If the new value of χ^2 is greater than the old one, we accept it if the ratio of the likelihood functions $L(\chi^2_{\text{new}})/L(\chi^2_{\text{old}}) > p$, where $p \sim \mathcal{U}(0, 1)$. We continue drawing samples until we get a total of $\hat{n} = 10^4$ samples. For the samples generated, we omit the first 1000 samples of the chain from our analysis.

With our generated samples, we can use the best fit, χ^2_{min}, to find the 1σ and 2σ confidence regions. For the χ^2 distribution with 3 parameters, these regions are given by $\chi^2 - \chi^2_{\text{min}} < 3.53$ and $\chi^2 - \chi^2_{\text{min}} < 8.02$, respectively. We will plot the 1σ and 2σ constraint in the $(\Omega_{m0}, \Omega_{\Lambda 0})$ plane. Since $\Omega_{r0} < 10^{-4}$, $\Omega_{\Lambda 0}$ can be approximated well by $\Omega_{\Lambda 0} = 1 - \Omega_{m0}$. After that we will plot the posterior probability distribution function (PDF) for H_0. When presenting the best fit parameters, we include both the standard deviation of each parameter in C, and the quantity χ^2_{min}/N, where $N = 31$ as previously stated. The latter can be used to validate the goodness of the fit, as this quantity will be close to unity if the fit is good.

To compare our fit with the Planck data, we will plot $d_L^{\text{obs}}(z_i)$ together with $d_L^{\text{fit}}(z)$ and $d_L^{\text{Planck}}(z)$. We obtain the former by solving the background cosmology with h, Ω_{m0}, Ω_{k0} replaced by the configuration $\hat{h}$, $\hat{\Omega}_{m0}$, $\hat{\Omega}_{k0}$ that yielded the lowest value of χ^2.

3.3. Results

In this section we present the results from our numerical simulations. Most of our results concern the evolution of various parameters as a function of x. Whenever it's relevant for interpreting and understanding the plot, we mark the point where we have matter-radiation equality and matter-dark energy equality, corresponding to $\Omega_m = \Omega_r$ and $\Omega_m = \Omega_\Lambda$, respectively. These points can be seen directly in Fig. 3.

3.3.1. Analytical and numerical comparisons

The dimensionless quantity $\eta \mathcal{H}/c$ is shown in Fig. 1. At the lowest values of $x \lesssim -10$, we see that $\eta \mathcal{H}/c = 1$, as expected. Slightly before matter-radiation equality takes place, we see a slight increase towards higher x. As we approach higher x, Ω_Λ starts dominating, and the solution eventually diverges, as expected.
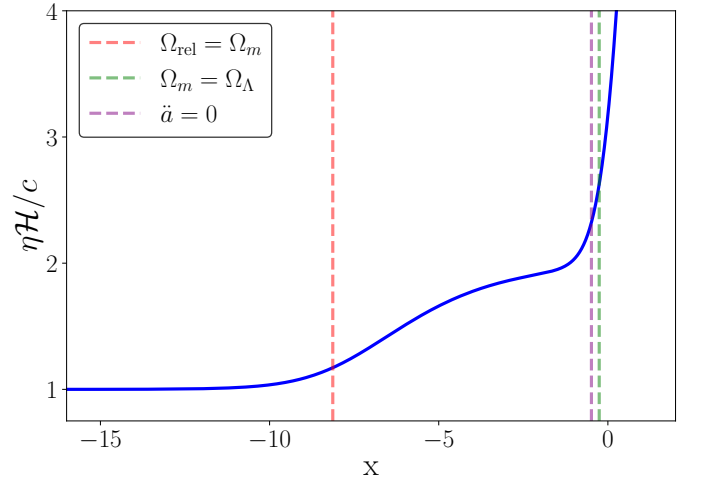
Fig. 1. The dimensionless quantity $\eta \mathcal{H}/c$ as a function of x. At low x it has a value of 1, as expected. The most significant changes occur near regions where there is a change in which density parameter is dominating.

In Fig. 2 we have plotted $\mathcal{H}'/\mathcal{H}$ and $\mathcal{H}''/\mathcal{H}$, where we include the analytical approximation from Eq. (29) and Eq. (30), respectively. The different values of w are drawn over the whole range of x where their related density parameter is larger than the other two. This is done for visibility purposes, and we only expect approximations to be reasonable whenever a density parameter is close to 1.
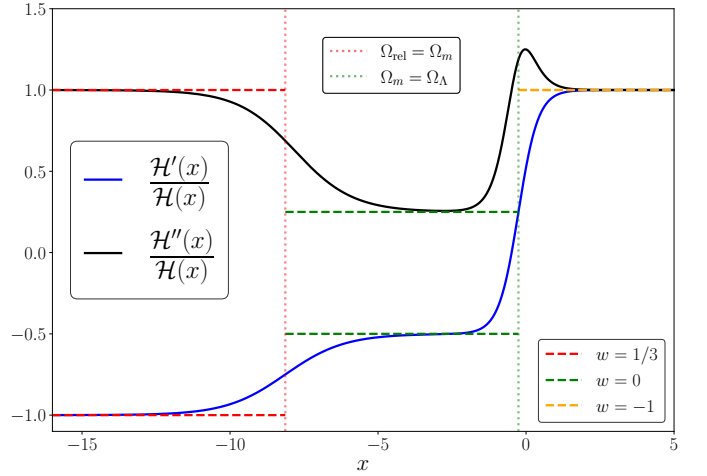

Fig. 2. $\mathcal{H}'/\mathcal{H}$ and $\mathcal{H}''/\mathcal{H}$ compared with analytical expressions in the case a single fluid with a given EoS parameter, w, shown by the dashed lines. The transition between the dashed lines are chosen as the corresponding epochs of equality.

Towards the smallest values of x we see that both quantities are well approximated by the analytical solutions for $w = 1/3$. As we reach $x \gtrsim 12$, matter becomes increasingly dominant, and the solution deviates from being purely dominated by a $w = 1/3$ fluid. Towards the highest values of x, we see that both quantities reach a constant value of 1 for $w = -1$. At higher values of x, we know that both $\Omega_m(x)$ and $\Omega_r(x)$ should vanish, eventually, while $\Omega_\Lambda \to 1$. This behaviour is thus present in our implementation. When matter dominates, we see that both functions exhibit inferior agreement with the approximations compared to the other regimes. This can be understood from Fig. 3, where

the vanishing contribution of Ω_r occurs around the same time as Ω_Λ starts contributing. The maximum value reached for this particular configuration is $\Omega_m \approx 0.995$. Nonetheless, significant deviations from the analytical solutions are not evident.
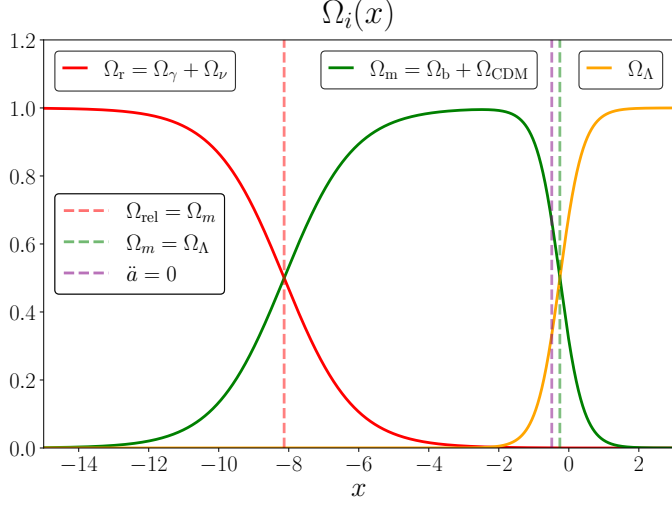

Fig. 3. Evolution of the density parameters over time. The points where $\Omega_m = \Omega_r$ marks the epoch of matter-radiation equality, and the intersection between Ω_m and Ω_Λ marks the epoch of matter-dark energy equality. The sum of the three quantities never exceed 1, as expected.

3.3.2. Hubble factor and time variables

Having checked that our implementation is physical, we now proceed by studying the evolution of the background, starting with a plot of the conformal Hubble factor, $\mathcal{H}(x)$, show in Fig. 4.

The local minima taking place before matter-dark energy equality corresponds to the onset of acceleration, where $\ddot{a} = 0$. For $x > 0$, Ω_Λ will dominate the conformal Hubble factor, where we have $\mathcal{H}(x) \propto e^x$, as seen from Eq. (8).
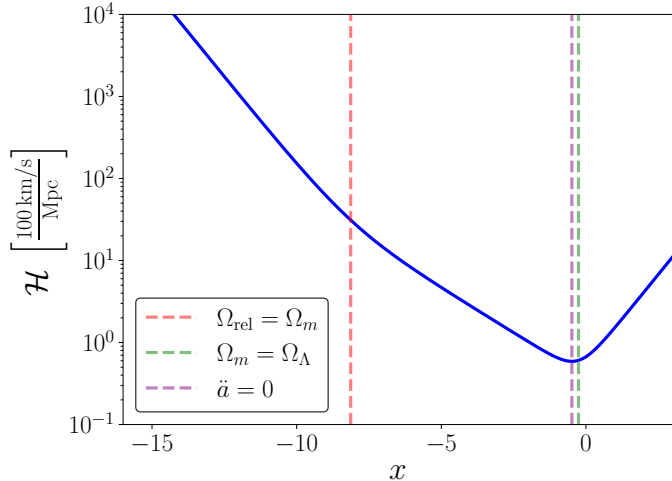

Fig. 4. Evolution of the conformal Hubble factor. The minimum point marks the onset of acceleration, after which, dark energy dominates its evolution.

The evolution of $\eta(x)$ and $t(x)$ is shown in Fig. 5. At high values of x, the e^x dependence of $\mathcal{H}(x)$ causes $\eta(x)$ to grow as

e^{-x} at late times, suppressing its growth. The cosmic time, on the other hand, does not have an exponential dependence in the integrand at high values of x. This yields the linear growth we see at late times. The different x-dependece of t and η results in the two quantities to be approximately equal at $x \sim 2.75$.
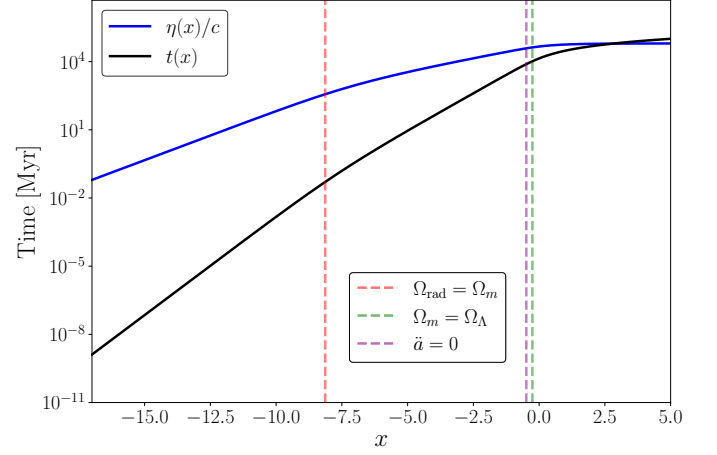

Fig. 5. The cosmic time, t and conformal time η/c. We emphasize that $\eta \neq t$ at small x, but the difference is discernable on the scale considered.

3.3.3. Supernova fitting

The best fit parameters are given in table 1, where the standard deviation of each parameter is included as a measure of the uncertainty. For Ω_{m0} and Ω_{k0}, we see that the best fit values are within one standard deviation from the measured Planck values. For H_0 on the other hand, this is not the case. The best fit yields $\chi^2_{\min}/N = 0.945$. This is close to unity, meaning that the fit is good. However, since it's smaller than one, this indicates that we are somewhat overfitting the data, but to confirm this, further analysis on the data is needed.

Table 1. The parameter values resulting in the lowest value of χ^2, obtained from fitting to supernova data.

Parameter	Best Fit
$\hat{H}_0$	$70.189 \pm 0.644\,\mathrm{km/s/Mpc}$
$\hat{\Omega}_{m0}$	0.259 ± 0.1111
$\hat{\Omega}_{k0}$	0.067 ± 0.2768
$\chi^2_{\min}/N$	0.945

Fig. 6 shows three luminosity distances, with observational data shown in red. The two curves shows the luminosity distance computed with Planck cosmology, dashed green line, and the result from using the parameters in table 1, solid blue line. We plot $d_L(z)/z$ to better compare the simulations with the data. There is a noticeable discrepancy between the data and the Planck cosmology, with most of the simulated values lying outside the measurement uncertainties. The simulation with the best fit parameters yields a luminosity distance function that is much more consistent with data. However, there is still some discrepancy at lower redshift, but the associated data points in this regime have large uncertainties.

The 1σ and 2σ confidence regions in the $\Omega_\Lambda - \Omega_m$ plane is shown in Fig. 7. In the figure we have also indicated the parameter configuration for a flat Universe. From this plot, it's evident
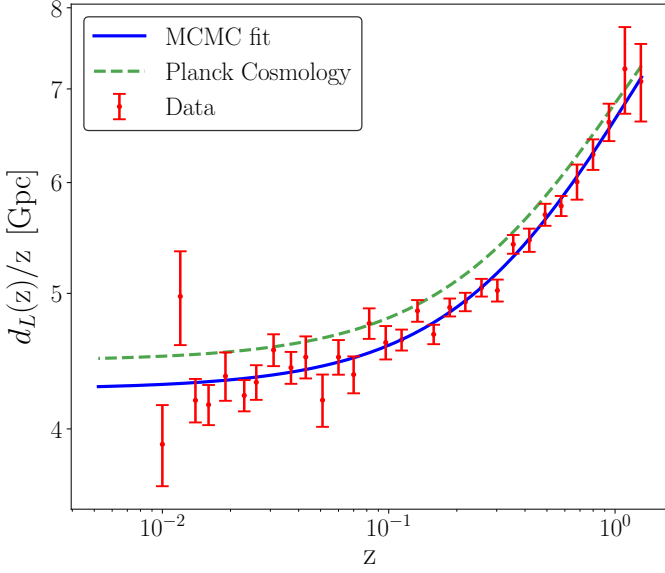
Fig. 6. The luminosity distance function obtained from the best fit values of C (blue line), compared with the result from the Planck cosmology (dashed green line).

that Planck cosmology is within 1σ region for the two density parameters, as the 1σ region covers a relatively large configuration space.
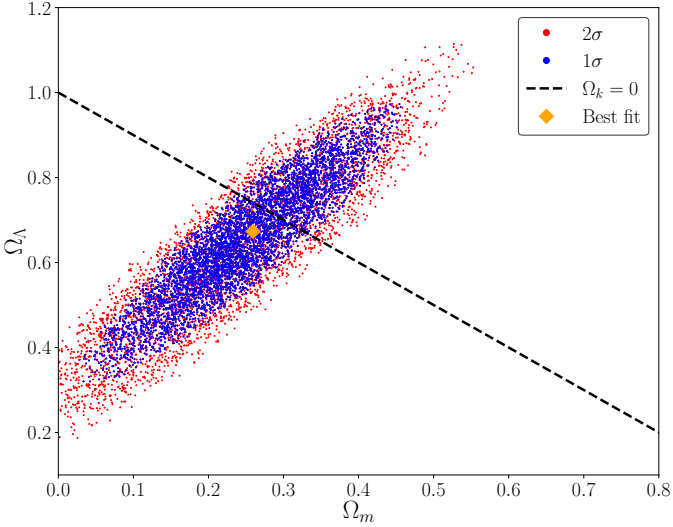

Fig. 7. Confidence regions of Ω_{m0} and $\Omega_{\Lambda 0}$ obtained from fitting the supernova data. The best fit parameter values are shown in the plot, as well as the configurations that would give a flat Universe.

The posterior PDF of H_0 is shown in Fig. 8, where we have included the resulting Gaussian distribution from the mean and variance of the sampled H_0 values. This shows distinct discrepancy from the value of $H_0 = 67$ km/s/Mpc, given by Planck. The minimum value of H_0 included in the accepted parameters is $\min(\hat{H}_0) = 67.58$ km/s/Mpc, meaning that the Planck value is not included at all.

There are three important periods we have discussed, the times of matter-radiation equality, acceleration onset and matter-dark energy equality. The times when these incidents occur are listed in table 3.3.3, in terms of x, redshift z and cosmic time t.
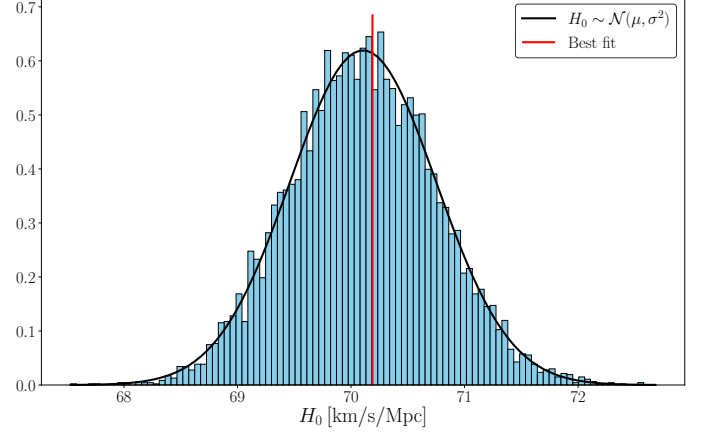
Fig. 8. Posterior PDF of H_0. The histogram shows the sampled values, while the blue curve is the corresponding normal distribution obtained from the mean and variance of the data.

We also include the age of the Universe today, $t_0 \equiv t(x = 0)$, and the conformal time today, η_0/c.

4. Milestone II

Having successfully implemented the background cosmology, the next step in developing our model is to include interactions between particles. After the Big Bang, the early universe was highly ionized. Due to Thompson scattering, photons were strongly coupled to baryons. As the Universe expanded, and the temperature dropped, neutral atoms were able to form, and the photons were able to escape from the plasma. These are the CMB photons we observe today. The period where neutral atoms formed is called recombination, and will be the main topic of this section. Our goal is to compute the number density of free electrons in the Universe, and use this to estimate when recombination occurred. The evolution of free electrons will affect both structure formation and the resulting power spectrum of the CMB photons, as we will study later.

We will use both the Saha and Peebles equation to compute the electron number density, and use this to compute the optical depth. From the optical depth, we will compute the so-called *visibility function*. Additionally, we will make the assumption that Hydrogen is the only element present in the universe. Hence, we use $Y_p = 0$, rather than the value from Planck, given in Eq. (2).

In this section, and for the remainder of this report, we adapt natural units, where we set $c = \hbar = k_B = 1$.

Eq. (1), as we neglect Helium and heavier elements.

4.1. Theory

4.1.1. Optical depth and visibility function

A source that emits light with an intensity I_0 is attenuated by a factor $e^{-\tau(x)}$ as it travels through a medium, where τ is the optical depth of the medium. In the early universe we have $\tau \gg 1$, and the universe is said to be optically thick. As the universe expands and recombination takes place, the universe becomes optically thin, $\tau \ll 1$, and light is able to escape the primordial plasma and reach us. Considering Thompson scattering only, the optical depth is defined in terms of the scale factor, a, as (Callin 2006,

	Matter-radiation equality $\Omega_m = \Omega_r$	Acceleration onset $\ddot{a} = 0$	Matter-dark energy equality $\Omega_m = \Omega_\Lambda$
x	−8.132	−0.487	−0.256
z	3400.3	0.627	0.291
t [Gyr]	51 028.9 yr	7.750	10.371

Age of Universe today:	$t_0 = 13.848\,\mathrm{Gyr}$
Conformal time today:	$\eta_0/c = 46.287\,\mathrm{Gyr}$

Table 2. Important times during the evolution of the Universe, expressed in terms of x, redshift and cosmic time. In the last two rows we also present today's time values

Eq. (5))

$$\tau(\eta) = \int_\eta^{\eta_0} \mathrm{d}\eta'\, n_e \sigma_T a, \tag{34}$$

where n_e is the number density of free electrons,

$$\sigma_T = \frac{8\pi\alpha^2}{3m_e^2} = 6.6524587158 \cdot 10^{-29}\,\mathrm{m}^2 \tag{35}$$

is the Thompson cross-section and a is the scale factor. α is the fine-structure constant and m_e is the electron mass. Using Eq. (15), we can rewrite Eq. (34) as a differential equation

$$\frac{\mathrm{d}\tau}{\mathrm{d}x} = -\frac{n_e \sigma_T}{H}, \tag{36}$$

which we can solve numerically once we know n_e. The initial condition is $\tau(x = 0) = 0$, as we then integrate over a medium of zero extent. The quantity τ' can loosely be viewed as a cosmological scattering rate, as it gives a measure of the number of scatterings a photon undergoes over the course of a Hubble time H^{-1}. In Sect. 6 we discuss how this quantity is crucial to understanding small scale features of the CMB.

From the optical depth, we obtain the so-called *visibility function* (Callin 2006, Eq. (8))

$$\tilde{g}(x) = -\tau' e^{-\tau}, \tag{37}$$

which has the property

$$\int_{-\infty}^0 \mathrm{d}x\, \tilde{g}(x) = 1. \tag{38}$$

This implies that $\tilde{g}(x)$ can be interpreted a probability distribution, namely the probability of an observed CMB photon today having experienced its last scattering at a time x. The visibility function is sharply peaked around the time when the photons decouple from the baryons, and is often referred to as the surface of last scattering. We may therefore use the peak of $\tilde{g}(x)$ to estimate the time when decoupling took place in the early universe. The time when recombination and decoupling takes place marks the time of when the Universe became transparent. In the very early Universe, the optical depth was high, meaning that no photons were tightly coupled to baryons, and thus not able to travel unimpeded. The time of decoupling thus marks the earliest period of the Universe that we are able to observe today. The CMB photons we observe today is therefore light emerging from the plasma at a time when $\tau \sim 1$. How the optical depth evolves is thus crucial to understand and compute the evolution of the early Universe, which is the topic of the next two sections.

4.1.2. Electron density

The final thing we need to compute τ and $\tilde{g}$ is the number density of free electrons. To compute the evolution of free electrons, we have to consider the Boltzmann equation (Dodelson 2020, Eq. (3.19))

$$\frac{\mathrm{d}f}{\mathrm{d}t} = C[f], \tag{39}$$

where f is the distribution function and $C[f]$ is a collision term.

We will consider the zeroth order of the Boltzmann equation, which is the relevant equation for the scope of our analysis of recombination. Following the notation and definitions from (Dodelson 2020, Eq. (4.5)-(4.9)), the equation we consider is given as

$$a^{-3}\frac{\mathrm{d}(n_1 a^3)}{\mathrm{d}t} = n_1^{(0)} n_2^{(0)} \langle\sigma v\rangle \left\{ \frac{n_3 n_4}{n_3^{(0)} n_4^{(0)}} - \frac{n_1 n_2}{n_1^{(0)} n_2^{(0)}} \right\}, \tag{40}$$

where n_i denotes the number density of a particle species i, with $n_i^{(0)}$ referring to its value in chemical equilibrium, and $\langle\sigma v\rangle$ is the thermally averaged cross-section. The only reaction we will consider for recombination is

$$e^- + p^+ \leftrightarrow H + \gamma. \tag{41}$$

For the photons we will assume $n_\gamma = n_\gamma^{(0)}$. From now on we use e and p as subscripts to denote free electrons and protons, respectively, and a subscript H to denote neutral Hydrogen.

Instead of computing n_e directly, we will compute the fractional electron density

$$X_e \equiv \frac{n_e}{n_e + n_H} \approx \frac{n_e}{n_b}, \tag{42}$$

where n_b is the total baryon density of the universe. Since the universe must be electrically neutral, we have $n_e = n_p$, and assuming no heavier elements than Hydrogen gives $n_b \approx n_p + n_H$. Neglecting the small mass difference between the proton and the Hydrogen, the baryon density can be written as

$$n_b \approx \frac{\rho_b}{m_H} = \frac{\Omega_{b0}\rho_{c0}}{m_H a^3}, \tag{43}$$

where $\rho_{c0} \equiv \frac{3H_0^2}{8\pi G}$ is the critical density of the universe today and m_H is the Hydrogen mass.

Before recombination occurs, the interaction rates greatly exceed the expansion rate of the universe, and for Eq. (40) to be valid we must have that

$$\frac{n_e n_p}{n_H} = \frac{n_e^{(0)} n_p^{(0)}}{n_H^{(0)}}. \tag{44}$$

In terms of X_e, this reduces to the Saha equation

$$\frac{X_e^2}{1 - X_e} = \frac{1}{n_b} \left(\frac{m_e T_b}{2\pi} \right)^{3/2} e^{-\epsilon_0/T_b}, \tag{45}$$

where T_b is the temperature of the baryons, and ϵ_0 is the Hydrogen ionization energy. The time evolution of T_b is governed by a differential equation coupled to X_e. However, we will assume that it follows the photon temperature, T_γ, evolving as

$$T_b = T_\gamma = T_{\text{CMB0}} e^{-x}. \tag{46}$$

At later times, Eq. (44) is no longer a valid approximation, and we have to solve Eq. (40). Additionally, we have to take processes related to atomic physics into account, so the differential equation we will consider is the Peebles equation

$$\frac{dX_e}{dx} = \frac{C_r(T_b)}{H} \left[\beta(T_b)(1 - X_e) - n_H \alpha^{(2)}(T_b) X_e^2 \right], \tag{47}$$

where $C_r(T_b)$, $\beta(T_b)$ and $\alpha^{(2)}(T_b)$ are quantities related to interaction effects, and are given by

$$C_r(T_b) = \frac{\Lambda_{2s \to 1s} + \Lambda_\alpha}{\Lambda_{2s \to 1s} + \Lambda_\alpha + \beta^{(2)}(T_b)}, \tag{48a}$$

$$\Lambda_{2s \to 1s} = 8.227 \, \text{s}^{-1}, \tag{48b}$$

$$\Lambda_\alpha = H \frac{(3\epsilon_0)^3}{(8\pi)^2 n_{1s}}, \tag{48c}$$

$$n_{1s} = (1 - X_e) n_H, \tag{48d}$$

$$\beta^{(2)}(T_b) = \beta(T_b) e^{3\epsilon_0/4T_b}, \tag{48e}$$

$$\beta(T_b) = \alpha^{(2)}(T_b) \left(\frac{m_e T_b}{2\pi} \right)^{3/2} e^{-\epsilon_0/T_b}, \tag{48f}$$

$$\alpha^{(2)} = \frac{64\pi}{\sqrt{27\pi}} \frac{\alpha^2}{m_e^2} \sqrt{\frac{\epsilon_0}{T_b}} \phi_2(T_b), \tag{48g}$$

$$\phi_2(T_b) = 0.448 \ln(\epsilon_0/T_b). \tag{48h}$$

The main reason behind these additional equations is that Hydrogen production is inefficient at $T_b \simeq \epsilon_0$. Direct recombination to the Hydrogen ground state is likely to produce a photon with energy greater than ϵ_0, which will ionize another nearby Hydrogen atom, resulting in no net Hydrogen production. Recombination is achieved when an electron and proton combine to an excited Hydrogen atom, followed by the atom's decay into the ground state, which is a slow process.

In Sect. 4.2.2 we discuss how combine the Saha and Peebles equation to compute X_e.

4.1.3. Sound Horizon at decoupling

Before recombination happens, baryons and photons are tightly coupled. For this reason, the baryons and photons behave as if they were a single fluid, and the sound speed of this fluid is given by (Dodelson 2020, Eq. (9.21)) (where we use $R \to 1/R$)

$$c_s(x) = \frac{c}{\sqrt{3}} \sqrt{\frac{R(x)}{1 + R(x)}}, \quad R(x) = \frac{4\Omega_\gamma(x)}{3\Omega_b(x)}. \tag{49}$$

The total co-moving distance a sound wave in this plasma could have travelled since the Big Bang is known as the sound-horizon, which is given as

$$s(x) = \int_{-\infty}^{x} \frac{dx' c_s}{\mathcal{H}}. \tag{50}$$

From this we can compute the sound horizon at decoupling, $r_s = s(x_{\text{rec}})$, which is an important quantity of the CMB. Thus, we have an additional ODE to solve,

$$\frac{ds(x)}{dx} = \frac{c_s}{\mathcal{H}}, \tag{51}$$

with $s(x_{\text{ini}}) = \frac{c_s(x_{\text{ini}})}{\mathcal{H}(x_{\text{ini}})}$ as the initial condition, following the same reasoning as we did for $\eta'(x)$ in Eq. (16).

4.2. Implementation details

To compute X_e, we use the Saha equation initially, as it is a good approximation at early times when $X_e \approx 1$. This is also the regime where the Peebles equation is unstable, and we therefore consider the Saha equation for $X_e > X_e^{\text{tol}}$. Once we reach $X_e < X_e^{\text{tol}}$ we use the final value from the Saha equation as our initial condition to solve the Peebles equation. The Peebles equation is then used all the way to today, at $x = 0$. For this report, we choose $X_e^{\text{tol}} = 0.99$. For comparison with the Saha equation alone, we set $X_e^{\text{tol}} = 10^{-6}$. Once X_e is computed we get $n_e(x)$ from Eq. (42).

4.2.1. Solving the Saha Equation

Solving the Saha equation is done by solving a quadratic formula for X_e. At early times, however, the RHS of Eq. (45) will be enormous, and may cause numerical errors when solving the quadratic formula. To avoid this, we use the first order approximation $\sqrt{1 + x} \approx 1 + \frac{x}{2}$ for $|x| \ll 1$ at early times. The Saha equation is thus implemented as

$$X_e = \begin{cases} 1, & y > 10^7, \\ \frac{y}{2} \left[-1 + \sqrt{1 + 4/y} \right], & y \le 10^7, \end{cases} \tag{52}$$

where y refers to the RHS of Eq. (45). Since X_e is strictly positive, we have omitted the negative solution. The exact value of 10^7 is chosen to ensure both $X_e \not> 1$, and $X_e \not< X_e^{\text{tol}}$ when the quadratic formula is to be used.

4.2.2. Solving the Peebles Equation

To solve Eq. (47) numerically, we follow the same procedure as we did for $\eta(x)$, but for the initial condition we use the final value of X_e that we obtained from the Saha equation.

At late times, when the baryon temperature gets low, the exponent term in Eq. (48e) for $\beta^{(2)}(T_b)$ become sufficiently large to yield an overflow. However, this is also where $\beta(T_b) \to 0$, due to its exponential factor (Eq. (48f)). This exponential factor causes $\beta^{(2)}(T_b) \to 0$ at late times. To avoid overflow, we implement the equation for $\beta^{(2)}(T_b)$ as

$$\beta^{(2)}(T_b) = \begin{cases} 0, & \epsilon_0/T_b > 200, \\ \beta(T_b) e^{3\epsilon_0/4T_b}, & \epsilon_0/T_b \le 200. \end{cases} \tag{53}$$

4.2.3. Optical depth and visibility function

With n_e we can then solve Eq. (36) for $\tau(x)$ with the aforementioned initial condition of $\tau(x = 0) = 0$. We therefore integrate backwards, starting from $x = 0$. The visibility function is now easily obtained, as $\tau'(x)$ is given analytically by Eq. (36). From this, we get immediately $\tilde{g}(x)$.

We also need the second derivative of τ, as well as the first two derivatives of $\tilde{g}$. For $\tau''(x)$, we compute it from numerically differentiating the $\tau'(x)$ data. We use this to compute

$$\tilde{g}'(x) = \left(\tau'(x)^2 - \tau''(x)\right) e^{-\tau(x)}, \tag{54}$$

and obtain $\tilde{g}''(x)$ by numerically differentiating $\tilde{g}'(x)$. This is done to avoid potential errors that may occur when numerically computing the second derivative of $\tilde{g}(x)$, if $\tilde{g}(x)$ is somewhat ill-behaved at certain times.

4.2.4. Determining the time of recombination and decoupling

To estimate the times when recombination takes place, we define this as

$$X_e(x = x_{\text{rec}}) = 0.1, \tag{55}$$

where the value $X_e = 0.1$ is chosen arbitrarily.

For decoupling, we find x_{dec} as the point where $\tau(x_{\text{dec}}) = 1$.

4.3. Results

4.3.1. Electron fraction

The evolution of the electron fraction with time is shown in Fig. 9. Here, we have included the solution obtained through the Saha equation alone for comparison. In the figure we also show the time periods when recombination occurs according to the two solutions, i.e. when $X_e = 0.1$. The time of decoupling has been omitted, since it is very close to the recombination time, as shown in table 3.

We see that the Peebles equation predicts the production of neutral Hydrogen to take much longer time than the Saha equation. As previously discussed, recombination occurs at a much lower temperature than the binding energy of Hydrogen, even with the Saha approximation, which does not take complicated atomic physics into account. Generally, the main reason for this delay is that the photons do not have a single energy, but rather a distribution of energies. The vast number of photons in the Universe means that at $T \ll \epsilon_0$, there are many photons available to ionize Hydrogen atoms, thereby delaying recombination. Towards $x = 0$ the Peebles equation give $X_e \ll 1$, which appears to settle at an approximately fixed value. From our solution we find that the current value is $X_e(x = 0) \approx 2.026 \cdot 10^{-4}$. On the other hand, the Saha equation yields a rapidly decaying electron fraction, with $X_e \ll 10^{-4}$ occurring long before $x = 0$ is reached.

4.3.2. Optical depth and visibility function

The optical depth, and its first two derivatives is shown in Fig. 10. We see that the three quantities rapidly drop by several orders of magnitude near $x = -7$, around the time of recombination. Looking at Fig. 11 we see that the rapidly varying optical depth results in a sharply peaked $\tilde{g}$.

4.3.3. Times of recombination and decoupling

The period of recombination and decoupling, as computed from the Peebles equation, is given in table 3. We see that the photons and baryons decouple later than recombination occurs, as is expected. This does depend on how we define the two periods, and is thus not a very conclusive result on its own. Using a higher value of X_e for instance would yield a larger separation between the two events.
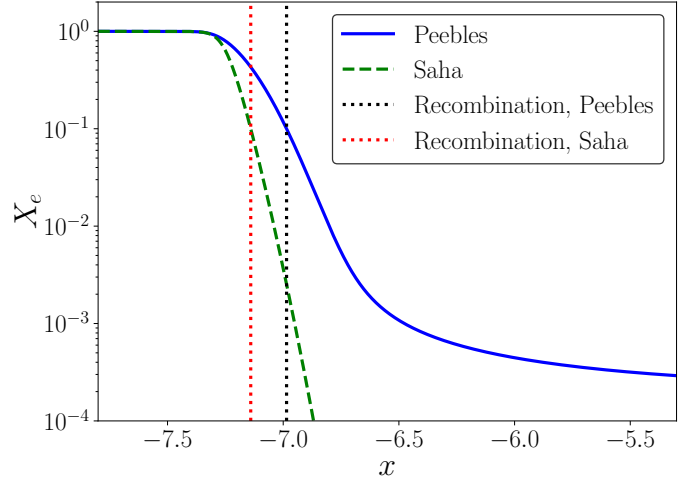

Fig. 9. Free electron fraction computed from the Saha equation only (dashed green curve) and from the Peebles equation (solid blue curve), where the Saha equation was used at early times, until $X_e < 0.99$. The recombination times is shown for both solutions.
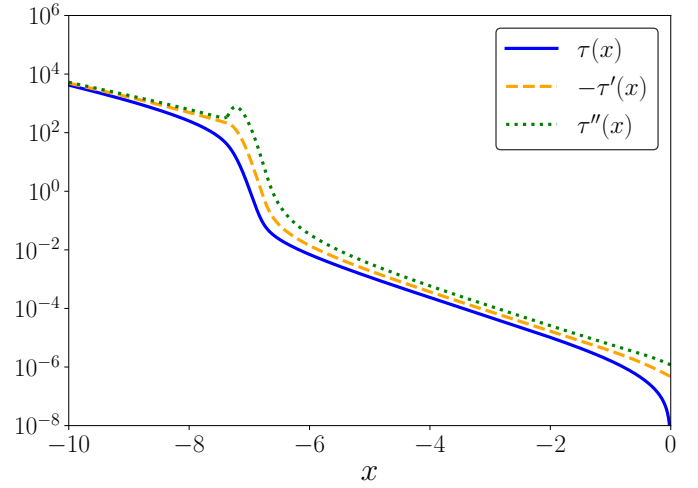

Fig. 10. The optical depth, $\tau(x)$ and its two first derivatives with respect to x.

Table 3. Times when decoupling, $\tau = 1$ and recombination, $X_e = 0.1$, occurs, computed from the Peebles equation.

Peebles	x	z	t [yr]	r_s [Mpc]
Decoupling	-6.98777	1082.3	376 242	145.08
Recombination	-6.98549	1079.8	377 690	

5. Milestone III

So far we have only considered the flat FLRW metric for a homogeneous Universe, and used this to study the recombination history of the Universe. In this section we will consider small perturbations to the background, and thereby introduce inhomogeneities. We will consider perturbations to the FLRW metric and the matter contents of the Universe, where we limit ourselves to photons, baryons and CDM. We will restrict ourselves to linear perturbations only, which allows us to derive good approximations for the Boltzmann and Einstein equations. From this we are able to study the evolution of structure in the early Universe, which we later will connect to statistical observables in
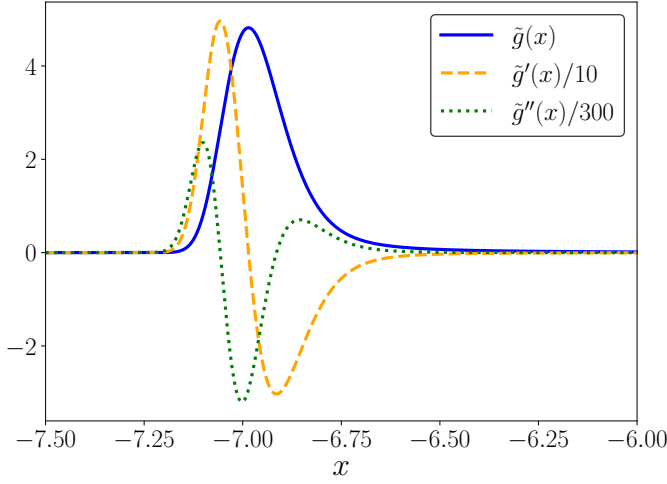
Fig. 11. The visibility function, $\tilde{g}(x)$ (solid curve), and its derivatives, $\tilde{g}'(x)/10$ (dashed curve) and $\tilde{g}''(x)/300$ (dotted curve). The derivatives have been scaled in order to view them all in the same plot.

Table 4. Times when decoupling, $au = 1$ and recombination, $X_e = 0.1$, occurs, computed from the Saha equation.

Saha	x	z	t [yr]
Decoupling	-7.15809	1283.5	282 051
Recombination	-7.14035	1260.9	290 686

the Universe. This means that we ignore contributions from neutrinos and polarization. This means that we set $\mathcal{N}_{\text{eff}} = 0$ when we compute relevant quantities from Sect. 3 and Sect. 4 that we will need in this section.

5.1. Theory

In this section we present the equations governing the evolution of the perturbed quantities. We will only present the relevant equations here, which are all obtained from Dodelson (2020) and Callin (2006), unless otherwise stated. We refer to Dodelson for a detailed derivation of the equations. For the notation, we adapt that of Callin. Throughout this section, we will consider perturbations in Fourier space.

5.1.1. Perturbation quantities

For the perturbed metric we consider the Newtonian gauge, and write it as

$$g_{\mu\nu} = \begin{pmatrix} -(1 + 2\Psi) & 0 \\ 0 & a^2\delta_{ij}(1 + 2\Phi) \end{pmatrix}, \tag{56}$$

where we have introduced the scalar perturbations Ψ and Φ, which are functions of both position and time. For $\Psi = \Phi = 0$ we obtain the FLRW metric. Photon perturbations are defined in terms of the relative temperature variations, $\Theta \equiv \delta T/T$, via

$$T(\boldsymbol{k}, \mu, \eta) = T^{(0)}(\eta)\left[1 + \Theta(\boldsymbol{k}, \mu, \eta)\right], \tag{57}$$

where $\boldsymbol{k}$ is the Fourier transformed variable corresponding to position $\boldsymbol{x}$, and $\mu \equiv \frac{\boldsymbol{k}\cdot\boldsymbol{p}}{kp}$. The temperature perturbations only depend on the photon momentum in terms of their directions, and we

therefore expand Θ in terms of multipoles as

$$\Theta_\ell = \frac{i^\ell}{2}\int_{-1}^{1}\mathcal{P}_\ell(\mu)\Theta(\mu)\,\mathrm{d}\mu \Leftrightarrow \Theta(\mu) = \sum_{\ell=0}^{\infty}\frac{2\ell+1}{i^\ell}\Theta_\ell\mathcal{P}_\ell(\mu), \tag{58}$$

where $\mathcal{P}_\ell(\mu)$ are Legendre polynomials. The first three multipoles are the monopole, Θ_0, the dipole, Θ_1 and the quadrupole, Θ_2. The monopole represents the background temperature of the CMB and the dipole represents our relative velocity with respect to the CMB.

We denote density perturbations of CDM and baryons as δ_{CDM} and δ_b, and their velocity perturbations as v_{CDM} and v_b. From the perturbed Einstein equations one can show that $\delta_\gamma = 4\Theta_0$ and $v_\gamma = -3\Theta_1$ for the photons.

5.1.2. Perturbation equations

The system of ODEs we will solve for the evolution of the perturbed quantities are given in (Callin 2006, Eq. (22)), where we neglect neutrinos and polarization and set $\Theta_P = \mathcal{N} = 0$.

$$\Theta_0' = -\frac{k}{\mathcal{H}}\Theta_1 - \Phi', \tag{59a}$$

$$\Theta_1' = \frac{k}{3\mathcal{H}}\Theta_0 - \frac{2k}{3\mathcal{H}}\Theta_2 + \frac{k}{3\mathcal{H}}\Psi + \tau'\left[\Theta_1 + \frac{1}{3}v_b\right], \tag{59b}$$

$$\Theta_\ell' = \frac{\ell k}{(2\ell+1)\mathcal{H}}\Theta_{\ell-1} - \frac{(\ell+1)k}{(2\ell+1)\mathcal{H}}\Theta_{\ell+1}$$
$$+ \tau'\left[\Theta_\ell - \frac{1}{10}\Pi\delta_{\ell,2}\right], \quad 2 \le \ell < \ell_{\text{max}}, \tag{59c}$$

$$\Theta_\ell' = \frac{k}{\mathcal{H}}\Theta_{\ell-1} - c\frac{(\ell+1)}{\mathcal{H}\eta(x)}\Theta_\ell + \tau'\Theta_\ell, \quad \ell = \ell_{\text{max}}, \tag{59d}$$

$$\delta_{\text{CDM}}' = \frac{k}{\mathcal{H}}v_{\text{CDM}} - 3\Phi', \tag{59e}$$

$$v_{\text{CDM}}' = -v_{\text{CDM}}\frac{k}{\mathcal{H}}\Psi, \tag{59f}$$

$$\delta_b' = \frac{k}{\mathcal{H}}v_b - 3\Phi', \tag{59g}$$

$$v_b' = -v_b - \frac{k}{\mathcal{H}}\Psi + \tau'R(3\Theta_1 + v_b), \tag{59h}$$

$$\Phi' = -\Psi - \frac{k^2}{3\mathcal{H}^2}\Phi + \frac{H_0^2}{2\mathcal{H}^2}[\Omega_{\text{CDM0}}a^{-1}\delta_{\text{CDM}} + \Omega_{b0}a^{-1}\delta_b$$
$$+ 4\Omega_{\gamma0}a^{-2}\Theta_0], \tag{59i}$$

$$\Psi = -\Phi - \frac{12H_0^2}{k^2a^2}\Omega_{\gamma0}\Theta_2. \tag{59j}$$

We have $\Pi = \Theta_2$ due to $\Theta_P = 0$, and have written Π for clarity. The equation for Ψ is an algebraic equation, and its value is inserted in the other equations. Noting that Φ' is the only derivative of a perturbed quantity found on the RHS of Eqs. (59), we solve for it first, and insert this value into the other equations.

In Sect. 6 we discuss the main topic of this report, which is to compute the power spectrum, C_ℓ, which involves integrating over Θ_ℓ. Since we are interested in probing the power spectrum at scales where $\ell > 1000$, we need a vast number of photon multipoles. From the ODE, we see that Θ_ℓ' is recursive, and computing Θ_ℓ directly from the ODEs will thus require us to solve thousands of ODEs. This is a highly tedious and computationally expensive process. However, as we will explain in Sect. 6.1.3, by exploiting the line-of-sight (LOS) integration technique Seljak & Zaldarriaga (1996), we can compute any order of Θ_ℓ for

$\ell > 2$ from Θ_0 and Θ_2. Thus, we only need to use the ODEs to accurately compute Θ_0 and Θ_2. For this, we need to truncate the series at some point. Truncating the series by setting $\Theta_{\ell_{\max}} = 0$ would lead to numerical errors propagating down to Θ_2. Eq. (59d) comes from assuming $\Theta_\ell(k, \eta) \sim j_\ell(k\eta)$ at high ℓ, where $j_\ell(k\eta)$ is the spherical Bessel function, and using the recurrence relation for j_ℓ (see Callin 2006, Eq. (46)-(49)). By an appropriate choice of $\ell_{\max}$, we greatly reduce the number of ODEs needed to accurately compute C_ℓ.

At early times, the optical depth is very high, since the mean free path of photons is much smaller than the horizon sizes we want to consider. In this regime, only the monopole and dipole are relevant, as higher order multipoles are heavily suppressed (Dodelson 2020, Eq. (9.12)). With momentum and pressure as the only relevant parameters to describe the photons, they essentially behave as a fluid. Their frequent collisions with electrons imply that the electrons and photons behave as one fluid. This is referred to as the *tight coupling regime*. We have a large value of $|\tau'|$ during tight coupling, so the photons scatter frequently over the course of a Hubble time, H^{-1}. On small scales, this implies that temperature gradients are washed out, since photons reaching an observer from a distance of approximately one mean free path, may originate from other regions in the plasma after several scatterings events have taken place. Hence, electrons are only affected by the nearest photons, and the system is therefore in thermodynamic equilibrium. The implications of the tight coupling regime results in the ODEs in Eq. (59) to become numerically unstable, and we have to resort to approximations. This is discussed in the next section.

5.1.3. Initial conditions

We will use adiabatic initial conditions, and follow the convention used by Winther (2023), with $f_\nu = 0$ as we omit neutrinos[1]. The set of ODEs we solve are linear, so we can choose a particular normalization, which we adjust for when computing the Power spectrum later on. The initial conditions are

$$\Psi = -\frac{2}{3}, \tag{60a}$$

$$\Phi = -\Psi, \tag{60b}$$

$$\delta_{\text{CDM}} = \delta_b = -\frac{3}{2}\Psi, \tag{60c}$$

$$v_{\text{CDM}} = v_b = -\frac{k}{2\mathcal{H}}\Psi, \tag{60d}$$

$$\Theta_0 = -\frac{1}{2}\Psi, \tag{60e}$$

$$\Theta_1 = \frac{k}{6\mathcal{H}}\Psi. \tag{60f}$$

The large value of τ' during tight coupling means that the terms proportional to τ' in Eq. (59) can be neglected, implying that $\Theta_\ell = 0$ for $\ell \geq 2$. However, we need the lowest non-zero contribution from these multipoles when numerically integrating the system of ODEs. By expanding in terms of $k/\mathcal{H}\tau' \ll 1$ and using the initial conditions, one can obtain the following expression for the higher order multipoles

$$\Theta_2 = -\frac{20k}{45\mathcal{H}\tau'}\Theta_1, \tag{61a}$$

$$\Theta_\ell = -\frac{\ell}{2\ell + 1}\frac{k}{\mathcal{H}\tau'}\Theta_{\ell-1}. \tag{61b}$$

[1] Note that Winther has a sign error in his expression for the initial condition for Ψ

These are the expressions we will use to compute the multipoles during tight coupling. Note that we $\Theta_1 \simeq -v_b/3$ in this regime. To avoid numerical instability when multiplying this with τ' in Eq. (59b) we derive a modified expression for Θ_1' and v_b' in Sect. 5.2.1. Furthermore, we discuss in that section how we determine when to stop using the tight coupling approximation.

5.1.4. Evolution of different modes

The evolution of a single mode is governed by Eq. (59). As the horizon grows, causal physics affects perturbations on increasingly larger scales. Initially we have $k\eta \ll 1$, and all modes are outside the horizon. As η grows, more and more modes enter the horizon. The epoch in which a mode enters the horizon affects its evolution. To study the evolution of perturbations, we focus on three different modes: one short-wavelength mode that enters the horizon during radiation domination, one large-wavelength mode that enters the horizon during matter domination, and one mode of intermediate scale.

Defining x_{entry} as $k\eta(x_{\text{enter}}) = 1$, we choose the wavenumbers

$$k \in \{0.001, 0.03, 0.3\}/\text{Mpc},$$
$$x_{\text{enter}} \in \{-5.182, -9.726, -12.098\}, \tag{62}$$

where the first and last element of x_{enter} correspond to modes entering the horizon when $\Omega_m \approx 0.95$ and $\Omega_\gamma \approx 0.95$, respectively. The intermediate mode will enter when $\Omega_m \approx 0.25$ and $\Omega_\gamma \approx 0.25$. We postpone the details regarding evolution of these modes to Sect. 5.3.

5.2. Implementation details

5.2.1. Tight coupling regime

During tight coupling, Eq. (63c) needs to be modified to avoid numerically instability at early times. Following Callin, the tight coupling regime is computed with

$$\varrho q = -[(1 - R)\tau' + (1 + R)\tau''](3\Theta_1 + v_b)$$
$$- \frac{k}{\mathcal{H}}\Psi + (1 - \frac{\mathcal{H}'}{\mathcal{H}})\frac{k}{\mathcal{H}}(-\Theta_0 + 2\Theta_2) - \frac{k}{\mathcal{H}}\Theta_0', \tag{63a}$$

$$v_b' = \frac{1}{1 + R}\left[-v_b - \frac{k}{\mathcal{H}}\Psi + R(q + \frac{k}{\mathcal{H}}[-\Theta_0 + 2\Theta_2 - \Psi])\right], \tag{63b}$$

$$\Theta_1' = \frac{1}{3}(q - v_b'), \tag{63c}$$

where we have introduced the parameter

$$\varrho = (1 + R)\tau' + \frac{\mathcal{H}'}{\mathcal{H}} - 1. \tag{64}$$

In the tight coupling regime we use the initial conditions given in Eq. (60). We then solve the ODEs given in Eq. (59), but compute Θ_1' and v_b' in the end by using Eq. (63). In this regime we use Eqs. Eq. (61a) and (61b) for Θ_2 and Θ_ℓ, respectively.

Next, we need to determine when the tight coupling approximation is valid. We use the same conditions as Callin, namely that the approximation holds as long as $|\tau'| > 10$ and $|k/\mathcal{H}\tau'| < 1/10$, and that it should not be used after the start of recombination. For the latter condition, we choose $x < -8.3$ as the time when recombination starts. If any of these three conditions fails, we switch to the full ODEs. We then use the final results from the tight coupling regime as initial conditions for the ODEs in Eq. (59), and integrate up to $x = 0$.

5.2.2. Integration of ODEs

When solving the perturbation ODEs we integrate across x for each mode k. We choose $N_k = 200$ logarithmically spaced values of $k \in [k_{min}, k_{max}]$, where $k_{min} = 5 \cdot 10^{-5}/\mathrm{Mpc}$ and $k_{max} = 0.3/\mathrm{Mpc}$. For the photon multipoles, we set $\ell_{max} = 7$.

Once the ODEs have been solved for all combinations of x and k, we make splines of the integrated perturbation quantities, except for Θ_ℓ for $\ell > 2$, as this will be solved using the LOS integration.

5.3. Results

In this section we present plots showing the evolution of some perturbation quantities. For the monopole and dipole, we express plot these in terms of δ_γ and v_γ, respectively. For easier comparison between evolution of baryons, photons and CDM, we plot CDM and baryons together in one figure, and baryons and photons together in another figure. In both cases we include all three modes in the same figure. This approach prevents cluttering, and helps us understand the interaction between the three constituents, as baryons interact with both CDM and photons.

In Figs. 12-16 we indicate the time of matter-radiation equality by a dotted black vertical line. We stress that matter-radiation equality occurs at $x_{eq} = -8.6577$, as opposed to the time given in table 3.3.3, since $\mathcal{N}_{eff} = 0$ now. The time of decoupling and recombination, however, is less affected, occurring at $x \sim -6.98$ as before. We also mark the horizon entry time for each mode, given in Eq. (62), shown as dash-dotted lines. For brevity, we will refer to modes with large k as *short modes* and modes with small k as *long modes*, as they are related to small and large scales, respectively.

We begin by studying the density evolutions in Sect. 5.3.1, and spend a considerable time interpreting these results qualitatively. This discussion provides a simpler way of understanding the mechanism behind the remaining perturbation quantities.

5.3.1. Density perturbations

The absolute value of the density evolution of baryons, CDM and photons is shown in Fig. 12, where the upper panel shows δ_{CDM} and δ_b and the lower panel shows δ_b and δ_γ. Before any of the modes enter the horizon, the baryons and CDM behave identically. For the two shorter modes, δ_b begins deviating noticeably from δ_{CDM} as upon entering the horizon. For the CDM, the growth of the density perturbation is due to CDM clustering as they undergo gravitational collapse, taking place around the time when the modes enter the horizon. This attracts baryons, which fall into the CDM potential wells. As baryons collapse, pressure from photons increases and pushes them outwards again. This phenomenon is apparent in the lower panel, where δ_b and δ_γ have the same evolution before decoupling takes places at $x \sim -7$. This process repeats for the two shorter modes, which have entered the horizon before recombination begins. When decoupling takes place, the photon pressure is unable to prevent gravitational collapse, and baryons fall into the gravitational wells set up by CDM. Consequently, δ_b follows δ_{CDM} at late times. The photons can move freely after decoupling, and their temperature remains approximately unaffected towards $x = 0$. Having oscillations in time Fourier space, this corresponds to moving plane waves in real space, which is why wee see some fluctuations in δ_γ at late times. There is also noticeable in δ_γ at $x \sim 0$ for the shortest mode. This is a result of accelerated expansion of the Universe at late times.

The evolution of the perturbations are largely affected by the current era of the Universe upon a mode's horizon entry, as we shall see in Sect. 5.3.3, but we state the main features here to better understand the behaviour of the perturbations. During radiation domination, photons exert pressure that prevents clustering. As a result, they can not counteract the effect of expansion, and for modes entering during radiation domination, the potentials decay as a result. The net effect of this decay (Dodelson 2020, Eq. (8.52)), is that CDM density perturbations grow as $\delta_{CDM} \propto \ln(k\eta)$. During matter domination on the other hand, accretion of matter is able to balance out the expansion of the Universe, and the potentials will therefore stay constant. This results in the steady growth we see in Fig. 12. At late times, accelerated expansion will cause the potentials to decay again, and clustering will therefore be halted.

In general, we see more oscillations in δ_b and δ_γ for smaller modes. The large mode enters the horizon long after decoupling, and the baryon overdensity is unaffected by photons when collapse begins. Neglecting terms with factors of k in Eq. (59), we get $\delta_b = \delta_{CDM}$ at all times, since they have identical initial conditions.

The value of δ_γ after decoupling differs between the three modes, where shorter modes have a lower final temperature. Decoupled photons are redshifted as they move out of gravitational potential wells. On small scales, where CDM have more time to cluster before decoupling, the escaping photons become more redshifted. Additionally, the actual evolution of the potential wells before decoupling is an important factor in the final photon temperatures. For the shortest mode, we see that δ_{CDM} grows differently right after horizon entry, compared to after x_{eq}. This is caused by the aforementioned effect of entering the horizon during radiation domination. The other two modes enter during matter domination, and does not experience this effect to a similar degree. As matter domination begins, all modes grow at roughly the same rate, as expected. Once again, we see the presence of acceleration towards $x = 0$, as the matter perturbations have a declining growth.

5.3.2. Velocity perturbations

The evolution of the velocities is shown in Fig. 13, where we compare baryons and CDM in the upper panel, and baryons and photons in the lower panel. Note that we have used a linear scale for the lower panel to reduce clutter.

In Fig. 12, the oscillatory behaviour of baryons for short modes is also apparent in their velocities, where the velocity extrema coincide with density minima, as expected, since a moving plane wave in real space corresponds to oscillations in Fourier space, with a velocity phase shifted by 90 degrees. Again, we see baryons and CDM coinciding at early and late times, as well as decoupling features present in between for the two shorter modes. For the longest mode, v_{CDM} and v_b follow the same argument as their densities, resulting in $v_{CDM} = v_b$.

For the shortest mode, v_{CDM} is no longer a strictly increasing function at early times. Around $x = -10$, v_{CDM} declines and becomes smaller than the intermediate mode around x_{eq}. The transition from radiation dominated to matter dominated growth of δ_{CDM} has resulted in a sufficient decrease in its velocity, but as matter domination becomes prominent, it evolves similarly to that of the other modes. For photons, we have $v_b \sim v_\gamma$ before decoupling, at $x \sim -7$. After that, the photons undergo damped oscillations, with the shorter modes having a higher frequency for shorter modes. The frequency differences are also present in Fig. 12, although less noticeable. These differences correspond
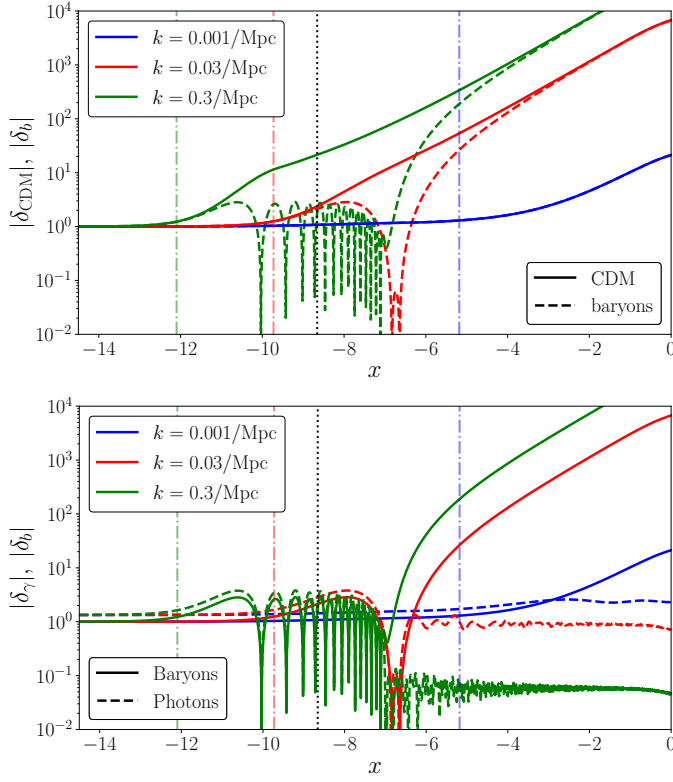
Fig. 12. Evolution of δ for modes with three different wavenumbers. Upper panel: Comparing δ_{CDM} (solid line) and δ_b (dashed line). Lower panel: Comparing δ_b (solid line) and $\delta_\gamma = 4\Theta_0$ (dashed line).
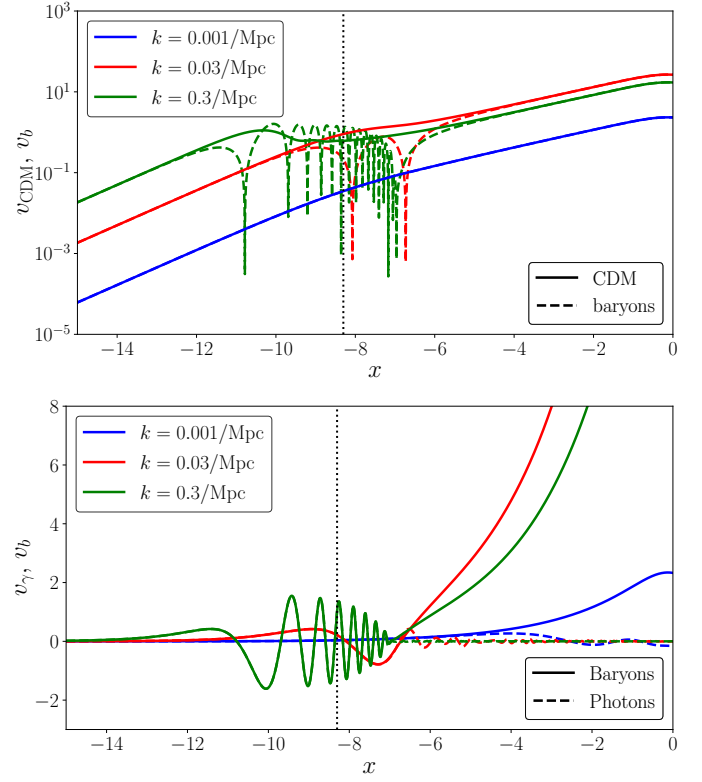
Fig. 13. Evolution of velocities for three different wavenumbers. Upper panel: v_{CDM} (solid line) compared to v_b (dashed line). Lower panel: v_b (solid line) compared to v_γ (dashed line).

to overdensities in real space being stretch outwards, with a velocity varying with radius.

5.3.3. Potential perturbations

The evolution of Φ is illustrated in Fig. 14. This analysis is based on the discussion presented in (Dodelson 2020, Ch. 8). During both matter and radiation domination, Φ can be well-approximated as being constant, with a transition period in between. As the shortest mode enters the horizon when $x \ll x_{eq}$, the potential decays and begins to oscillate, leading to the damped oscillations observed for photons and baryons in Fig. 12. As previously mentioned, the decay is a result of the expansion dominating accretion of matter. During matter domination, for a mode that has entered the horizon, we get a constant Φ, as the matter accretion is balanced by the Universe's expansion. However, we see that there is a distinct transition period between radiation and matter domination, particularly for the intermediate mode. This is mainly due to the energy density of radiation not vanishing completely after x_{eq}. As we shall see in Sect. 6, this will affect the temperature of the CMB photons. When decoupling takes place and photons travel towards us, when they pass through a time varying potential, their effective temperature will be changed upon arrival. The otherwise constancy of Φ during matter domination explains why all modes in Fig. 12 grow at the same rate at late times, long after decoupling. For the transition period of the shortest mode mentioned earlier, we can compare the changes in the growth of δ_{CDM} at points where Φ exhibits irregular behaviour. Most notably, the minima in Φ at around $x \sim -10$ roughly corresponds to the change in δ_{CDM} for the short mode at the same x. Similarly, this point is where we also had a slight reduction of v_{CDM}.
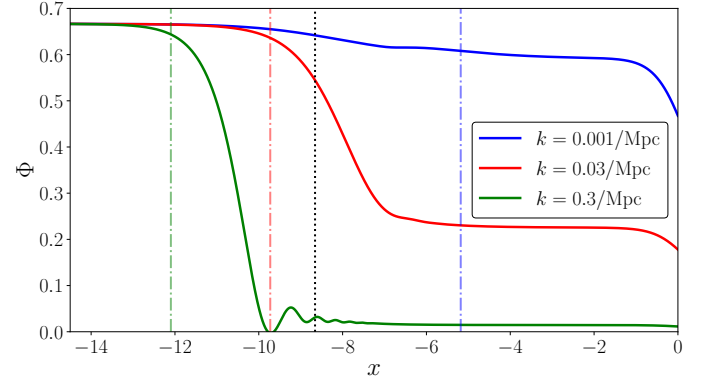

Fig. 14. Evolution of Φ.

The sum of the two metric potentials, $\Phi + \Psi$, is plotted in Fig. 15. This quantity corresponds to the second term on the right-hand side of Eq. (59j) and is proportional to the quadrupole moment, Θ_2, which is depicted in Fig. 16. Specifically, we have $\Phi + \Psi \propto -\frac{\Theta_2}{k^2}e^{-2x}$. Since $\Theta_2(x \ll x_{eq}) \approx 0$, the sum of the potentials is initially zero. Although the proportionality constant is very small, for larger x, late in the matter dominated era, there is a narrow range where both Θ_2 contributes and the exponent is large enough to give a non-zero contribution.

For the evolution of Θ_2, we first begin to see growing oscillations in the short mode around $x = x_{eq}$. This growth is abruptly suppressed once decoupling happens, where we also had an abrupt decrease of v_γ in Fig. 13. Similar behaviour is seen for the remaining two modes. For these modes, oscillations start around the time of decoupling, and continues with an ampli-

tude related to the amplitude of the oscillations of v_γ. The largest mode is also responsible for the largest value of Θ_2 at $x = 0$.

The evolution of Θ_2 is characterized by growing oscillations in the short mode around $x = x_{\mathrm{eq}}$, which are suddenly suppressed upon decoupling. This abrupt decrease is also seen as a decrease in v_γ in Fig. 13. Similar behaviour is also observed for the remaining two modes. Oscillations for these modes start around decoupling and persist with an amplitude that is related to the amplitude of v_γ oscillations. The largest mode exhibits the highest Θ_2 value at $x = 0$. One of the most interesting features of Θ_2, is that oscillations are not abruptly suppressed after decoupling, compared the monopole and dipole. In Sect. 6.1.3, we will see that Θ_2 directly affects the effective temperature of the CMB photons observed today.
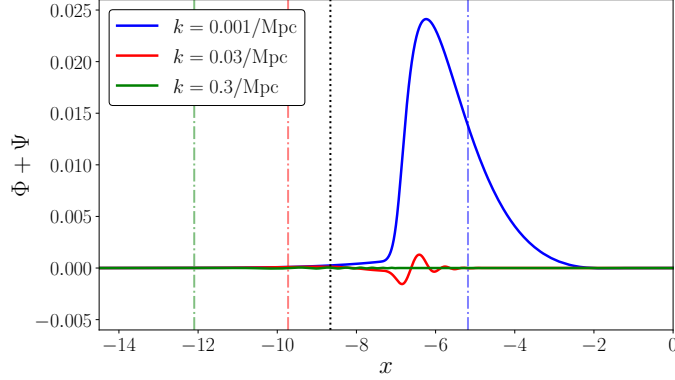

Fig. 15. Evolution of the combined metric perturbations, $\Phi + \Psi$
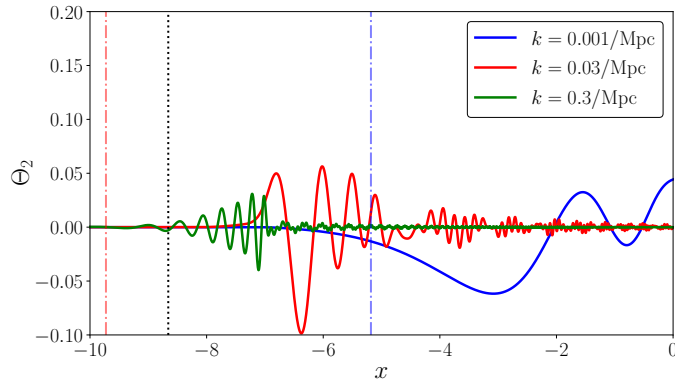

Fig. 16. Evolution of the quadrupole, Θ_2. At $x < -10$, there is no apparent contribution of this quantity.

6. Milestone IV

We now have all the necessary constituents needed to compute the main quantity of interest in the report, the CMB power spectrum. By expanding the temperature field in spherical harmonics, we will be able to exploit the line-of-sight (LOS) integration technique in order to efficiently compute multipoles up to $\ell = 2000$. From the multipoles, we will compute the CMB power spectrum, and compare this to observations from Planck experiments. By studying the power spectrum in some detail, we will also gain crucial physical insight into the various processes that determines the growth of structure in the early Universe.

We are concerned with both the angular power spectrum of the CMB, and the matter power spectrum. When only "power

spectrum" is written, we are referring to the former, and other power spectra will be referred to with appropriate prefixes. Most of our discussion of the physics behind various aspects of the power spectrum will be qualitative, where most is obtained from (Dodelson 2020, Ch. 9).

6.1. Theory

In this section, we begin by introducing the general theory behind how the CMB power spectrum is computed. Using these equations, we will derive some approximate results that relates to general features we expect to see. Based on this initial understanding of the power spectrum, a more detailed discussion is presented when discussing the results in Sect. 6.3.

6.1.1. Angular power spectrum

The temperature fluctuations can be expanded in spherical harmonics as

$$\Theta(\boldsymbol{x}, \hat{\boldsymbol{p}}, t) = \sum_{\ell=1}^{\infty} \sum_{m=-\ell}^{\ell} a_{\ell m}(\boldsymbol{x}, t) Y_{\ell m}(\hat{\boldsymbol{p}}), \tag{65}$$

where the amplitudes, $a_{\ell m}$, contain all the information about the temperature field, and are to be evaluated at our position in the Universe at $t = t_0$. However, we are unable to make prediction about particular values of these amplitudes, as inflation is a stochastic process. Since inflation predicts Θ to be very close to Gaussian, each $a_{\ell m}$ is therefore drawn from a normal distribution with zero mean and a variance given as

$$\langle a_{\ell m} a_{\ell' m'} \rangle = \delta_{\ell \ell'} \delta_{m m'} C_\ell, \tag{66}$$

where the brackets denote an ensemble average.

We follow the approach of (Dodelson 2020, Ch. 9.5), leaving out the details of the derivation. We now omit factors of t in the expressions, as we are only concerned with the value at $t = t_0$, and obtain

$$C_\ell = 4\pi \int \mathcal{P}_\mathcal{R}(k) \left| \Theta_\ell^{\mathrm{code}}(k) \right|^2 \frac{\mathrm{d}k}{k}, \tag{67}$$

where we have used $\Theta_\ell(\boldsymbol{k}) = \Theta_\ell^{\mathrm{code}}(k) \mathcal{R}_{\mathrm{ini}}$, where $\mathcal{R}_{\mathrm{ini}} \propto \Psi$ comes from inflation. This rescaling accounts for the fact that we have set $\Psi = -2/3$ as our initial condition when solving the perturbation ODEs numerically. $\mathcal{P}_\mathcal{R}(k)$ is related to the primordial power spectrum, $P(k)$, via

$$P(k) = \frac{2\pi^2}{k^3} \mathcal{P}_\mathcal{R}(k), \tag{68}$$

where $\left\langle \mathcal{R}_{\mathrm{ini}}(\boldsymbol{k}) \mathcal{R}_{\mathrm{ini}}^*(\boldsymbol{k}') \right\rangle = (2\pi^2)\delta(\boldsymbol{k} - \boldsymbol{k}')P(k)$. To compute C_ℓ, the last thing we need is an expression for $\mathcal{P}_\mathcal{R}(k)$. We get an expression for this from the fact that most inflationary models predict a spectrum on the form

$$\mathcal{P}_\mathcal{R}(k) = A_s \left(\frac{k}{k_{\mathrm{pivot}}} \right)^{n_s - 1}, \tag{69}$$

where A_s is the primordial amplitude, k_{pivot} is the scale where the amplitude of $\mathcal{P}_\mathcal{R}(k)$ is A_s, and n_s is the spectral index, determining how perturbations at different scales are affected by inflation. For $n_s = 1$ perturbations are scale invariant, whereas we have $n_s = 0.965$, meaning that the power spectrum will be tilted to give an increased amplitude on larger scales.

Thus, the final expression we want to compute is

$$C_\ell = 4\pi \int_0^\infty A_s \left(\frac{k}{k_{\mathrm{pivot}}} \right)^{n_s - 1} \Theta_\ell^2(k) \frac{\mathrm{d}k}{k}. \tag{70}$$

6.1.2. Matter power spectrum

From the Fourier components of the matter overdensity field, we can compute the matter power-spectrum

$$P_L(k, x) = |\Delta_M(k, x)|^2, \quad \text{where} \quad \Delta_M(k, x) \equiv \frac{k^2 \Phi(k, x)}{\frac{3}{2}\Omega_{m0}e^{-x}H_0^2}. \quad (71)$$

Once again, we have to take rescale Δ_M to account for our choice of initial conditions. Taking the value today, we thus want to compute

$$P_L(k) = \left|\Delta_M^{\text{code}}(k)\right|^2 P(k) = \left|\Delta_M^{\text{code}}(k)\right|^2 \frac{2\pi^2}{k^3}A_s\left(\frac{k}{k_{\text{pivot}}}\right)^{n_s-1}. \quad (72)$$

The shape of $P_L(k)$ is naturally divided into three regions. On small scales, modes enter the horizon during radiation domination, where the growth of perturbations is suppressed due to photon pressure. On larger scales, modes entering the horizon in the matter dominated era, or later, are not affected by this suppression. In between these two regimes, we expect there to be a scale k_{eq}, where $P_L(k)$ peaks. This equality scale is $k_{\text{eq}} \equiv \mathcal{H}(x_{\text{eq}})$. From Baumann (Ch. 5.2.3), we find the asymptotic behaviour of $P_L(k)$ as

$$P_L(k) \propto \begin{cases} k^{n_s}, & k < k_{\text{eq}}, \\ k^{-3}, & k > k_{\text{eq}}, \end{cases} \quad (73)$$

which encodes the physical differences of how different modes grow.

6.1.3. Line-of-sight integration

As mentioned in Sect. 5.1.2, we compute higher order multipoles from the LOS approach.

$$\Theta_\ell(k, x = 0) = \int_{-\infty}^{0} \tilde{S}(k, x)j_\ell[k(\eta_0 - \eta(x))]\,\mathrm{d}x, \quad (74)$$

where $j_\ell(k(\eta_0 - \eta(x)))$ is the spherical Bessel function. $\tilde{S}(k, x)$ is the source function, which is given by

$$\tilde{S}(k, x) = \tilde{g}\left[\Theta_0 + \Psi + \frac{1}{4}\Pi\right] + e^{-\tau}[\Psi' - \Phi']$$
$$- \frac{1}{k}\frac{\mathrm{d}}{\mathrm{d}x}(\mathcal{H}\tilde{g}v_b) + \frac{3}{4k^2}\frac{\mathrm{d}}{\mathrm{d}x}\left[\mathcal{H}\frac{\mathrm{d}}{\mathrm{d}x}(\mathcal{H}\tilde{g}\Pi)\right], \quad (75)$$

where $\Pi = \Theta_2$.

In order to gain insight into the impact of different physical effects on the power spectrum, we can examine the individual components of the source function. We will provide such an analysis of the individual components of $S(k, x)$, and their resulting C_ℓ, in Sect. 6.3.1. Before delving into those details, we begin by presenting a general overview of each term in the next section.

6.1.4. Physics behind the LOS integral

The main physical idea behind the LOS approach, is that light observed in a given direction from the CMB today, is directly related to the CMB monopole along the LOS from us to infinity. The four terms in the source function represent different physical effects, with the first two being the so-called Sachs-Wolfe (SW) term and the integrated Sachs-Wolfe (ISW) effect. As we will see later, SW is the dominant contributor to C_ℓ, so we neglect

the other terms for now. Since $\tilde{g}$ is a sharply peaked at recombination, we may approximate it as a delta function, giving

$$\Theta_\ell^{\text{today}}(k) \approx [\Theta_0 + \Psi + \Theta_2/4]_{\text{rec}} \cdot j_\ell(k(\eta_0 - \eta_{\text{rec}}))$$
$$\approx [\Theta_0 + \Psi]_{\text{rec}} \cdot j_\ell(k\eta_0), \quad (76)$$

where we have used $\eta_{\text{rec}} \ll \eta_0$, and the fact that $\Theta_2 \ll \Theta_0$ at recombination. The quantity $\Theta_0 + \Psi$ represents an effective photon temperature. As the decoupled photons travel freely towards us today, they are gravitationally redshifted by the potential, Ψ. Hence, the SW term is an effective photon temperature with a tiny quadrupole correction. The anisotropies observed in the power spectrum today originate from temperature irregularities that existed during recombination. These irregularities were frozen in during the decoupling process, and serve as indicators of the underlying physics prior to photon decoupling.

From the approximation in Eq. (76), we see that $\Theta_\ell \propto j_\ell(k\eta_0)$. Since $j_\ell(x)$ has a peak at $x \sim \ell$, we expect $\Theta_\ell(k)$ to have a peak at $k \sim \ell/\eta_0$. On small angular scales, the spherical Bessel function can be approximated as (Dodelson 2020, Eq. (9.61))

$$j_\ell(x) \xrightarrow{x/\ell \to 0} \frac{1}{\ell}\left(\frac{x}{\ell}\right)^{\ell-1/2}, \quad (77)$$

so when $x < \ell$, i.e. $k\eta_0 < \ell$, the spherical Bessel function is heavily suppressed. Consequently, the power spectrum at a particular ℓ receives minimal contribution from larger-scale modes where $k < \ell/\eta_0$. This behaviour can be easily understood from a physical perspective, as we anticipate limited anisotropy on small angular scales arising from perturbations characterized by large wavelengths. On the other hand, for angular scales $\ell < 1/(k\eta_0)$, there is also a negligible contribution to the photon multipole from j_ℓ. Thus, following Eq. (70), we may expect perturbation features on scales k to be mapped onto angular scales of $\ell \sim k\eta_0$ in C_ℓ. In Sect. 6.3.4 we will see an example of how various ℓ-values depend on k.

The ISW represents the fact that gravitational potentials may change in time as photons move through it. For freely moving photons entering gravitational potentials, there is no net change in temperature if the potentials remain constant in time. Photons entering a gravitational potential gets an energy change that is cancelled out by the energy change it experiences when it leaves the gravitational potential again, if the potential remains constant in time. The potentials are also weighted by a factor $e^{-\tau}$, so we only get a contribution from this term after recombination. Modes decaying after recombination are therefore expected to yield a noticeable ISW effect. From Fig. 14, we may expect contributions from intermediate scale modes on intermediate angular scales. On large scales, when the Universe starts accelerating, the potentials decay. With a low value of τ, on these scales we also expect contributions to C_ℓ from the largest angular scales, i.e. at low ℓ.

The third term in Eq. (75) is effectively a dipole term, since $v_b \sim v_\gamma$ at early times. From our discussion of the evolution of the monopole and dipole, in Fig. 12 and 13, we can expect the dipole term to contribute on scales that had entered the horizon before decoupling. Additionally, with Θ_0 and Θ_1 being out of phase, we expect anisotropies from this term to be out of phase with anisotropies of the SW as well. The final term is a quadrupole term, and is related to the angular dependence of Thompson scattering. However, as we will see in Sect. 6.3, this term gives a very small contribution.

An important aspect of C_ℓ, is its behaviour at large scales. If the ISW contribution is ignored, for low l, we have $(\Theta_0 + \Psi)_{\text{rec}} \approx$

$(\Theta_0 + \Psi)_{\text{ini}}$, since the large scale modes have not entered the horizon before decoupling. The SW term is therefore approximately given as $\Theta_\ell \approx (\Theta_0 + \Psi)_{\text{ini}} j_\ell(k\eta_0)$. Substituting $x = k\eta_0$, the integral in Eq. (70) for $n_s = 1$ becomes

$$C_\ell = 4\pi A_s |(\Theta_0 + \Psi)_{\text{ini}}|^2 \frac{1}{(k_{\text{pivot}}\eta_0)^{n_s-1}} \int_0^\infty \mathrm{d}x\, j_\ell^2(x) x^{n_s-2},$$

$$\implies \frac{\ell(\ell+1)}{2\pi} C_\ell = A_s |(\Theta_0 + \Psi)_{\text{ini}}|^2 = \text{constant}. \tag{78}$$

When plotting the CMB power spectrum, we will plot the RHS of Eq. (78) against ℓ in units of $\mu\mathrm{K}^2$, which is then expected to be roughly constant. We have $n_s = 0.965 < 1$, so we have $\ell(\ell+1)C_\ell \propto \ell^{n_s-1}$, which will induces a small tilt at low ℓ. The ISW will also result in a further deviation from a constant value.

6.2. Implementation details

One of the most crucial parts about integrating to obtain $\Theta_\ell(k)$ and C_ℓ, is that the quantities we're integrating are oscillating rapidly. We must therefore ensure that we have a sufficiently high resolution, so that we accurately sample the integrands.

6.2.1. LOS integration

We begin by computing the source function. For the distribution of k, we use the same configuration as we did in Sect. 5.2.2. We use a linear spacing of $x \in [-15, 0]$, with $N_x = 5000$ points, ensuring sufficient sampling at intermediate and late times when it becomes important. The result is splined then splined across k and x.

The second term needed for the LOS integration is the spherical Bessel functions. To increase efficiency when integrating Eq. (74), we create a spline of the Bessel functions. We consider the interval $\tilde{x} \in [0, k\eta_0]$, with a spacing of $\Delta\tilde{x} = 2\pi/n$ where $n = 32$, to ensure sufficient sampling in each period of the oscillations.

When computing $\Theta_\ell(k)$ for a given ℓ, the spacing in k is important to accurately integrate Eq. (67) later on. For $\Theta_\ell(k)$ we use a linear spacing in k, with $\Delta k = \frac{2\pi}{\eta_0 n}$ for $n = 32$. We use the same interval as we did in the source function, giving us a total of $N = 21\,773$ values of k. For each k and ℓ, Eq. (74) is integrated across x with a simple trapezoidal method. We use 2000 values of $x \in [-15, 0]$ for this. The resulting multipole values are stored in a 2D spline over k and ℓ.

From Eq. (75) we see that the integrand is approximately zero when $\tilde{g} = 0$ and τ is very large. This suggests that a natural way of increasing the efficiency of this calculation is to identify when the source function is non-zero, independent of k and ℓ, thus reducing the number of points needed to accurately compute $\Theta_\ell(k)$.

6.2.2. Computing the power spectrum

The integral in Eq. (67) can be computed by integrating over $\mathrm{d}k/k = \mathrm{d}\log k$. We therefore choose a linear spacing of logarithmic k-values, using the same resolution as we did for the LOS integration. We integrate using the trapezoidal rule once again, and store the final result on a spline.

6.3. Results

The resulting CMB power spectrum we obtain provides vital information on the main cosmological parameters we use today.

We will briefly discuss some parameter dependencies when relevant for the results we obtain. However, having mostly used the latest Planck values for the cosmological parameters, we will not discuss consequences of parameter adjustments in detail. With several degeneracies in this multidimensional parameter space makes it difficult to make detailed conclusions of parameter dependency, without explicit computations, which is too time-consuming to do at the moment.

6.3.1. CMB power spectrum

We begin our analysis by qualitatively explaining the most prominent features of the power spectrum. In particular, we make frequent use of Eq. (76), which offers as a simple way for gaining an initial understanding of the main features we observe in the power spectrum. We limit our initial discussion to only include effects that may be understood from the SW term mostly. After this initial discussion, we will explore the physics behind the results in greater detail.

The angular power spectrum is shown in Fig. 17, where vertical lines have been drawn to mark the position of the peaks (red) and troughs (blue). We include data from Planck Collaboration et al. (2020) for low ℓ values. At higher ℓ, neutrinos, helium and reionization becomes important, and our prediction of C_ℓ at small scales would deviate from that of observations.

The peaks we observe in the power spectrum result from the oscillations in the photon baryon plasma, seen in Sect. 5.3. Modes enter the horizon at different times, depending on their size, which affects the state of the plasma when the photons decouple. If the plasma is fully compressed upon recombination, the photons have to escape from deep potential wells, and will therefore be redshifted. Similarly, if a mode is fully decompressed at recombination, the photons are less redshifted as they escape the potential wells. Both of these extrema will result in a relatively large temperature inhomogeneity. Since C_ℓ depends on the absolute value of the photons multipoles, these extrema shows up as the peaks of the power spectrum. The troughs therefore correspond to modes for which the temperature perturbation is approximately zero. This will therefore occur when the oscillation is at its mean value, in between the extrema.

As seen in Sect. 5.3, the size of the modes strongly affect their behaviour before decoupling. Small scale modes will undergo several oscillations before recombination occurs. The number of oscillations a mode undergoes before decoupling decreases for larger scale modes, and for modes larger than the horizon during recombination, we expect no oscillations to take place. Thus, the peak at $\ell = 205$ corresponds to a mode that just began to oscillate, with recombination taking place when it was at its maximum. As ℓ is decreased from 205, the modes are gradually less compressed, until we reach scales of modes that had not entered the horizon before decoupling. On the largest angular scales, we see a manifestation of Eq. (78), as the power spectrum is roughly constant, as expected.

To see that the peaks and troughs in Fig. 17 actually correspond to modes where Θ_0 is at extrema, we plot $\Theta_0(k, x)$ as a function of x for $k = \ell_{\text{peak}}/\eta_0$ and $k = \ell_{\text{trough}}/\eta_0$, shown in Fig. 18. We also mark the region of $x \sim x_{\text{rec}}$. As evident from the figure, the first three peaks of C_ℓ correspond to modes on scales that are at maxima. The troughs occur at scales that are essentially zero deviation from the initial temperature perturbation. Modes with wavenumber $k \sim \ell_{\text{trough}}/\eta_0$ give roughly zero contribution to the power spectrum, but modes with different wavenumbers give a non-zero contribution to the power spectrum, effectively lifting the troughs.
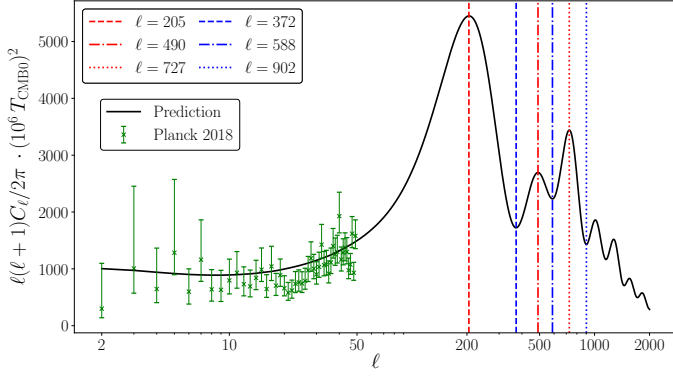
Fig. 17. The predicted CMB power spectrum (black) compared with data from Planck at large scales. Fix y-label. Should indicate T_{CMB0}

Another important feature, is that the maxima of $\Theta_0(x)$ in the upper panel of Fig. 18 don't occur at $x = x_{\mathrm{rec}}$. In general, inhomogeneities on scale k contributes to C_ℓ at slightly lower value of ℓ than $\ell = k\eta_0$. One reason for this, is that $j_\ell(x)$ peaks when ℓ is slightly smaller than x.
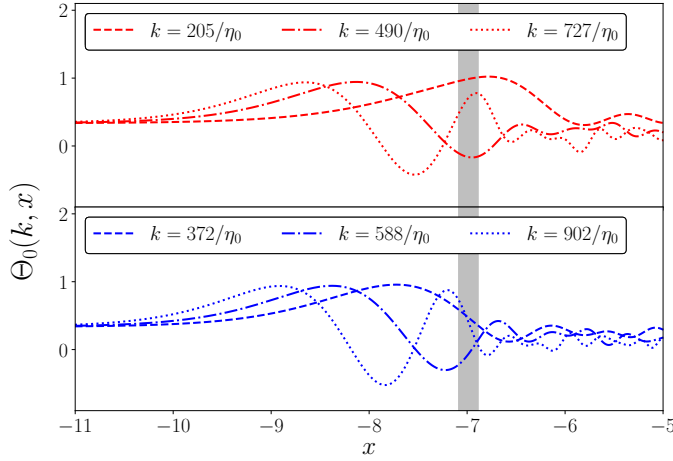

Fig. 18. Computed monopoles for of scale $k = \ell/\eta_0$ for different values of ℓ. The upper panel are ℓ values where the power spectrum peaks, and the lower panel are the ℓ values of the power spectrum troughs.

The next prominent feature in Fig. 17 are the damping of the peaks at small scales. During tight coupling, photons and baryons do not behave exactly as one fluid. In reality, photons travel a certain distance between scattering events, essentially performing random walks. During a Hubble time H^{-1}, a photon will scatter $N = |\tau'| = n_e \sigma_T / H$ times. With a mean free path of $\lambda_{\mathrm{MFP}} = 1/n_e \sigma_T$ for Thomson scattering, the mean distance a photon travels during a Hubble time is

$$\lambda_D = \lambda_{\mathrm{MFP}} \sqrt{N} = 1/\sqrt{n_e \sigma_T H}, \tag{79}$$

On scales smaller than λ_D, scattering has the effect of smoothing the temperature fluctuations, since photons diffuse over such a region, causing the region to have a single mean temperature. In phase space, this corresponds to a damping on small scales $k_D \gtrsim 2\pi/\lambda_D$. Although recombination is not an instantaneous process, it does occur relatively fast. There will be some random walks undertaken by photons as they decouple, but they will very rapidly start streaming in straight lines as n_e eventually becomes very small. For a mode with wavelength much larger than λ_D, an observer would measure photons coming in from all directions

from a distance $\lambda \sim \lambda_{\mathrm{MFP}}$, over which the temperature hardly varies. Thus, larger angular scales are not affected by diffusion of photons.

Diffusion explains the damping at large ℓ, and also helps us understand why the first peaks have much larger amplitudes than the others, as damping has a decreasing effect on larger scales. The peak at $\ell = 205$ is hardly affected at all, whereas the third experiences some damping effect, although not noticeable, since it is counteracted by another effect, as we explain later. The second peak experiences some damping, but the same effect that counteracts suppression of the third peak also induces significant suppression of the second peak. In addition to damping of higher peaks, there is an important effect which amplifies the peaks. The potentials of modes entering the horizon before matter domination, will decay, as seen in Fig. 14. This will amplify peaks when potentials decay during a compression phase, since the photon no longer has a potential to overcome upon escaping. Amplification on smaller scales is not sufficient to fully overcome diffusion on small scales, as the latter is an exponential suppression. Note that potential decaying affects the SW term as well as the ISW term. In Fig. 14, we see that the intermediate mode has a decaying potential when $\tau \gg 1$, and a potential that is almost constant when $\tau \lesssim 1$, which yields a negligible ISW effect. This decay however, will affect the effective photon temperature at decoupling.

We mentioned that the third peak is higher than the second peak, as opposed to the higher peaks, which are generally lowered at higher ℓ. This follows a general trait, namely that the odd numbered peaks are enhanced relative to the even peaks. Odd numbered peaks are caused by compressions, which occur when the baryon photon plasma falls into the gravitational wells set up by the CDM. However, as baryons fall into these potential wells, they will effectively make the potential well deeper. As a result, photons escaping from these potential wells during decoupling gets a further decrease in their effective temperature.

6.3.2. Contribution from individual components

In Fig. 19, we plot the power spectrum obtained from the four individual terms in Eq. (75). Note that the quadrupole term is non-zero, but has a negligible contribution to power spectrum compared to the other terms. It can be seen on a logarithmic scale, but we choose a linear scale to better understand how the other terms contribute to the overall power spectrum. We emphasize that the four individual terms in Fig. 19 don't sum up to C_ℓ, since cross terms in Θ_ℓ^2 are missing. The cross terms play an important role, and we can infer some of its implications from the isolated contributions alone.

The SW term is the dominant contribution to C_ℓ, which justifies the choice of considering this term only for the discussion in the previous subsection. The second most dominant term is the Doppler term. On the largest scales, $\Theta_1 \simeq 0$, since these modes have not entered the horizon prior to decoupling, resulting in decreasing contribution at lower ℓ. On smaller scales, we see that the dipole raises the overall spectrum, but it does so more for the troughs than the peaks. This is due to the monopole and dipole being out of phase, and the dipole therefore reduces the prominence of the peaks in the power spectrum. We previously argued that the troughs are non-zero due to non-zero monopole contributions from several modes. This argument still holds, as seen from the SW line in Fig. 19 (green line), but the dipole induces a considerable lifting of the troughs. Hence, the dipole term means that the contribution from a single mode will result in a non-zero trough.

The final main contributor to the power spectrum is the ISW term. As expected, it gives a contribution at low ℓ. Modes entering the horizon after decoupling have approximately constant potentials initially. As dark energy begins to dominate, the Universe begins accelerating, causing the potentials to decay, as seen from Fig. 14. These modes give a contribution to C_ℓ at low ℓ, and are referred to as the late time ISW effect. There is also a noticeable contribution at intermediate scales, known as the early ISW. The transition from radiation domination to pure matter domination is not an abrupt process, and radiation energy density is not completely negligible after recombination, as seen from Fig. 3. For modes where this decay lasts until $\tau \simeq 1$, we get a noticeable ISW effect.
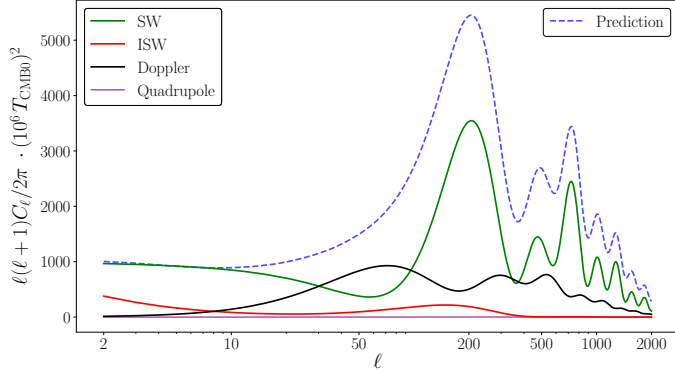

Fig. 19. The total angular power spectrum (dashed blue curve), compared to power spectra computed from individual terms in Eq. (75). For each term in the figure, the remaining terms in Eq. (75) have been set to zero.

The ISW appears to have a relatively small contribution to C_ℓ, compared to the dipole term. However, there is an important contribution coming from cross terms that we have ignored. In Fig. 19, we see that the ISW contribution is in phase with the SW contribution. The dipole on the other hand is out of phase with the SW term. The relative contribution from ISW to C_ℓ is therefore stronger than that from the dipole term.

6.3.3. Matter power spectrum

The matter power spectrum is plotted in Fig. 20. For comparison, we have included the result obtained from not having $\mathcal{N}_{\text{eff}} = 0$ in the background. This affects k_{eq}, as well as the value of Φ, since $\mathcal{H}$ is slightly altered by including neutrinos. We have not accounted for neutrinos when solving the perturbation ODEs, so this approach should only be taken as a highly approximate way of studying how neutrinos affect $P_L(k)$.

The behaviour of $P_L(k)$ follows that of Eq. (73). There is a noticeable discrepancy between the predicted value of $P_L(k)$ compared to that from data at high k. This regime is related to growth of perturbations on small scales, and is thus affected by the radiation at early times. Comparing with the prediction where neutrinos are included, we get a reduction of $P_L(k)$ on small scales, differing from the data by roughly the same magnitude. This does, nonetheless, seem reasonable. When neutrinos are ignored completely, matter domination begins earlier. Modes inside the horizon grows as $\Delta_M \propto \log(a)$ during radiation domination, while they grow as $\Delta_M \propto a$ during matter domination. Thus, small scale modes have been able to grow more, resulting in the difference between the predicted value of $P_L(k)$, in blue, and the observational data.

At small scales we also notice oscillating behaviour of $P_L(k)$. Before recombination, photons exert pressure on the baryons, dragging them outwards from the CDM potential wells. When photons eventually decouple, there is an excess of baryons around a spherical shell of the sound horizon, r_s, which is how far the baryons have been able to travel. Most of the baryons will follow the CDM, but a region of excess baryons will remain in place, starting to attract CDM as well. This clustering around r_s, caused by the photons, translates to oscillations in Fourier space, as seen in the low k end in $P_L(k)$.
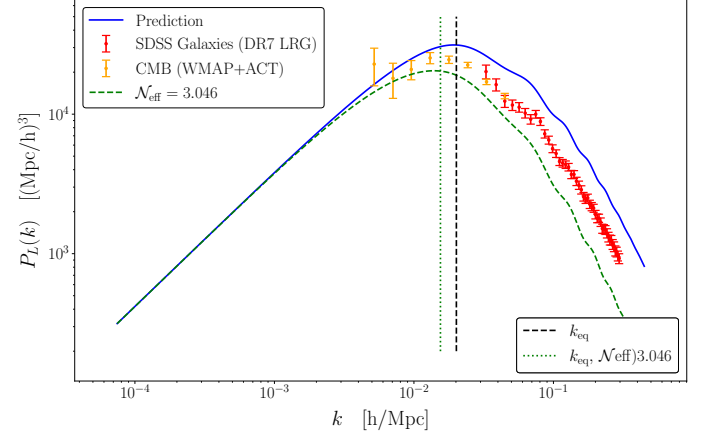

Fig. 20. Computed matter power spectrum (solid blue curve), compared with observational data from cite. The equality scale, k_{eq}, is marked as the vertical black line.

6.3.4. Photon multipoles

The transfer function, $\Theta_\ell^{\text{code}}(k)$, and the integrand term of C_ℓ, Θ_ℓ^2/k, is plotted for different values of ℓ, shown in Fig. 21 and Fig. 22, respectively. We stress that the files have been stored with a sampling of $N = 2000$ values of k, which is less than 10 % of the number of values used to both compute the transfer function and C_ℓ.

For the integrand in Fig. 21 we have plotted for $\ell = 20, 200$ and 300, and used a scaling of $\ell(\ell + 1)$, just as we did for C_ℓ, to better compare the different values. Towards higher k, it's evident that a high resolution is needed to obtain an accurate result. We note that all integrands die out very slowly, and a high resolution is thus important to sample the integrand properly upon integrating. Each graph peaks at $k\eta_0$ slightly larger than ℓ, as expected from our previous discussions. This suggests that a natural way to increase numerical efficiency would be to omit the lower k-values when computing the source function for a given ℓ. Comparing with Fig. 4 in Callin, we get a reasonably good agreement, regarding the overall shape and evolution of the integrands.

In Fig. 22, the aforementioned sampling issue is highly noticeable, with $N = 2000$ causing clear sampling issues. The sampling used in the actual computations seems to give reasonable results, based on Fig. 21, which does not show such prominent sampling issues. From the shape of the transfer functions alone, it appears that increasing the sampling by a factor of 10 could yield appropriate results.

7. Conclusions

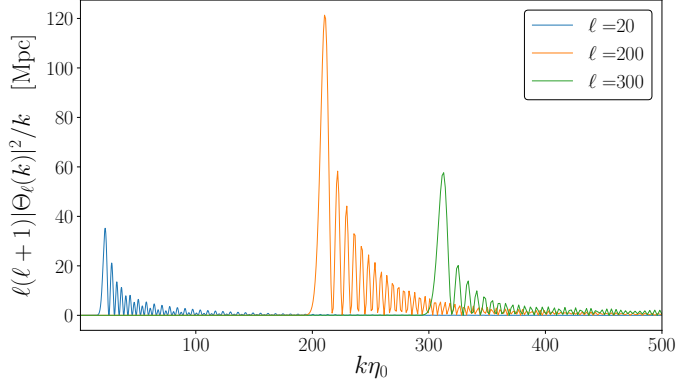Write a short summary and conclusion in the end.

Fig. 21. The term involved in the integrand of Eq. (70), for different values of ℓ. Note that we scale each integrand by $\ell(\ell + 1)$, just as we did for C_ℓ. This is done to see each of the terms simultaneously.
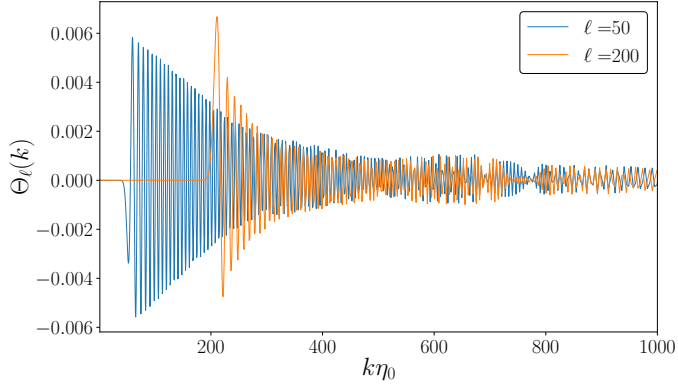

Fig. 22. The transfer function from Eq. (74) plotted for different values of ℓ.

References

Baumann, D. 2022, Cosmology (Cambridge University Press), doi: `10.1017/9781108937092`

Betoule, M., Kessler, R., Guy, J., et al. 2014, A&A, 568, A22, doi: `10.1051/0004-6361/201423413`

Callin, P. 2006, arXiv e-prints, astro, doi: `10.48550/arXiv.astro-ph/0606683`

Dodelson, S. 2020, Modern Cosmology (Academic Press), doi: `10.1016/C2017-0-01943-2`

Galassi, M. e. a. 2009, GNU scientific library reference manual (Network Theory Ltd.)

Planck Collaboration, Aghanim, N., Akrami, Y., et al. 2020, A&A, 641, A6, doi: `10.1051/0004-6361/201833910`

Seljak, U., & Zaldarriaga, M. 1996, ApJ, 469, 437, doi: `10.1086/177793`

Winther, H. A. 2023, Cosmology II: Initial conditions. `https://cmb.wintherscoming.no/theory_initial.php#init`